ELSEVIER

Contents lists available at ScienceDirect

## **Open Ceramics**

journal homepage: www.sciencedirect.com/journal/open-ceramics





# Thermodynamic stability of doped ceria for solar reactors: Sublimation and surface segregation

K.T. Streckel <sup>a,b,\*</sup>, L. Koch <sup>c</sup>, M. Müller <sup>d</sup>, M. Schmitkamp <sup>a</sup>, D. Sebold <sup>a</sup>, S. Baumann <sup>a</sup>, A. Nijmeijer <sup>b</sup>, W.A. Meulenberg <sup>a,b</sup>, N. Knoblauch <sup>c,\*</sup>

- a Forschungszentrum Jülich GmbH Institute for Energy Materials and Devices, Material Synthesis and Manufacturing Processes (IMD-2), Germany
- <sup>b</sup> University of Twente Faculty of Science and Technology, Inorganic Membranes (TNW-IM), Netherlands
- <sup>c</sup> Institute of Frontier Materials on Earth and in Space, German Aerospace Center, 51147 Cologne, Germany
- d Forschungszentrum Jülich GmbH Institute for Energy Materials and Devices, Structure and Function of Materials (IMD-1), Germany

#### ARTICLEINFO

#### Keywords: Solar-reactors Ceria Zirconia-doping

#### ABSTRACT

The stability of ceria-based redox oxides under high-temperature solar-thermal operation is crucial for fuel-producing reactors. This study demonstrates that the gas pressure governs  $CeO_2$  sublimation from  $Gd_{0.1}Ce_{0.9}O_{1.95}$  (GDC-10) under solar thermochemical conditions. Annealing GDC-10 at 1400 °C in vacuum ( $\approx 10^{-4}$  bar) produces a porous, sponge like surface layer enriched in Gd, confirming selective  $CeO_2$  sublimation; identical treatments in argon at the same temperature and duration do not generate comparable porosity. Time resolved electron microscopy reveal a diffusion controlled, linear growth of the cerium depleted zone, while dilatometry records irreversible chemical expansion, indicating structural damage. Co-doping with 5 mol % Zr  $(Ce_{0.9}Gd_{0.05}Zr_{0.05}O_{1.975})$  reduces  $CeO_2$  loss and yields a saturated surface. Knudsen effusion mass spectrometry shows reduced  $CeO_2$  volatility for the co-doped material after aging, linking thermodynamic stability to improved microstructural integrity. These results establish Zr co-doping as a potential strategy to stabilize GDC type redox oxides for durable solar thermochemical fuel production.

#### 1. Introduction

The quest for a sustainable energy future has brought hydrogen and its derivatives, such as synthetic hydrocarbons and ammonia, to the forefront as key elements in transitioning towards a greener economy, particularly in sectors that are challenging to decarbonize, like aviation. The production of hydrogen and synthetic hydrocarbons relies heavily on the splitting of carbon dioxide into carbon monoxide and water into hydrogen, as well as oxygen, with the subsequent removal of oxygen. This process enables the direct use of hydrogen or the production of hydrocarbons from syngas [1].

There are three primary methods for generating these essential components: electrolysis, solar thermochemical processes, and photoelectrochemical methods. Among these, electrolysis is the most advanced method for carbon dioxide and water splitting, especially when conducted at room temperature [1]. Photo-electrochemical processes also operate at room temperature and have the advantage of directly utilizing photons for the electrochemical reaction [2]. However, concentrated solar power can also be directly utilized in solar-thermal reactors, such as two-step thermochemical redox cycles and membrane reactors, which offer promising avenues for sustainable hydrogen and syngas production through the thermodynamic decomposition of water and carbon dioxide [1].

Two-step thermochemical redox cycles utilizing metal oxides have demonstrated high efficiency potential for water and carbon dioxide splitting, making them suitable for solar thermal fuel production [3]. These cycles involve alternating reduction and oxidation steps at different temperatures and require the development of transition metal oxide-based redox materials with oxygen storage and release properties [3]. Ceria, specifically CeO<sub>2</sub>, is the state-of-the-art material for both solar-thermal reactors with similar operation conditions, but its limited oxygen exchange capacity restricts the amount of  $\rm H_2$  produced per cycle [4]. Solar-thermal membrane reactors typically operate around 1500 °C with oxygen partial pressures of  $\rm 10^{-5}$  bar in argon [5–7] and for the redox cycles of starting at 1400 °C with total pressures of  $\rm 10^{-6}$  bar proceeding to around 700–800 °C for the oxidation [1,8,9]. Both techniques are currently in the focus of scale-up and commercialization efforts [9,10].

E-mail addresses: k.streckel@fz-juelich.de (K.T. Streckel), Nicole.Knoblauch@dlr.de (N. Knoblauch).

https://doi.org/10.1016/j.oceram.2025.100871

<sup>\*</sup> Corresponding authors.

Recent research has focused on enhancing fuel production by partially replacing Ce<sup>4+</sup> cations with other elements, particularly through isovalent substitution [3]. However, this approach increases reduction extent but slows down splitting kinetics and decreases thermodynamic favorability for water and carbon dioxide splitting [3,11]. Aliovalent substitution, particularly with trivalent dopants like lanthanides (e.g., Gd or La), has shown promising results, creating intrinsic oxygen vacancies that boost ionic conductivity and impact the kinetics of water or carbon dioxide splitting [3,12].

A recent alternative has proposed combining trivalent (e.g.,  $La^{3+}$ ,  $Y^{3+}$ ) and pentavalent dopants (e.g.,  $Nb^{5+}$ ) to mimic the effect of tetravalent cations, resulting in materials with higher efficiency for water splitting than Zr or Hf-doped ceria [13,14]. Despite these advances,  $CeO_2$  remains the preferred choice for scaling up processes in solar power demonstration plants due to its high reliability, achieving a record solar-to-syngas energy efficiency of 4.1 % without implementing heat recovery [15,16].

Nevertheless, investigations by Knoblauch et al. revealed that for doped ceria after heating up to 1673 K under low total pressure  $p=2\times 10^{-5}\,\mathrm{mbar}$ , significant changes can be observed on the sample surfaces. At higher temperatures,  $CeO_2$  is prone to evaporation, which is explained by its relatively higher vapor pressure compared to the doping ions. In fact, surface accumulation of doping ions can be detected due to this selective evaporation of  $CeO_2$ , which leads to a spongy-like porous surface zone of higher dopant composition. This surface enrichment of doping elements can, therefore, significantly slow down the re-oxidation kinetics of  $CO_2$  or  $H_2O$  splitting reaction due to the relatively decreasing ceria content and thereby degrade the long-term redox performance [17].

In this context, a deeper understanding of the thermodynamic stability of ceria-based materials at high temperatures is essential. Shugurov's recent studies have investigated the thermodynamic stability of  $CeO_2$ - $Gd_2O_3$  solid solutions using Knudsen effusion mass spectrometry (KEMS) in the temperature range 19,00-2300 K [18]. The results show that the thermodynamic most stable solid solution of ceria can be obtained in a binary system with  $ZrO_2$ .

Gadolinium-doped (GDC) ceria has been selected as the primary material for this study due to its use in both reactor systems and its presence as a commercial product. The global GDC electrolyte market size, valued at USD 474.2 million in 2024, is projected to experience substantial growth, reaching USD 1191.7 million by 2033, underscoring its increasing commercial relevance [19]. To illustrate the scale of GDC's application, based on a 2024 ceria price of approximately USD 3287 per metric ton [20], the annual production and usage of gadolinium-doped ceria can be estimated to be within the range of tens to low hundreds of thousands of metric tons.

The objective of this paper is to further investigate the porous surface that forms on  $Gd_{0.1}Ce_{0.9}O_{1.95}$  (GDC-10) under the described application-relevant conditions by annealing tests that are evaluated by SEM/EDS, Raman, and SIMS. Additionally, strategies to stabilize the surface, based on Knoblauch's and Shugurov's recent results by stabilization with Zr, are investigated, as well as their effects on the expansion and chemical expansion by dilatometry. Finally, KEMS measurements are performed to establish a linkage to the mechanism of Cerium vanishing on the surface.

## 2. Materials and methods

## 2.1. Sample preparation

GDC-10 ( $Ce_{0.9}Gd_{0.1}O_{1.95}$ ) was purchased from Solvay Special Chem Japan, Ltd. (Anan—City, Japan; Ref. No. 138879; surface area: 7.8 m²/g;  $D_{50}=0.16~\mu m$ ). The powder was uniaxially pressed into pellets (20 mm diameter  $\times$  1 mm thickness).

 $CeO_2$  (99.9 %,  $<5~\mu m,$  Lot MKCC8706) and  $Gd_2O_3$  (>99.9 %) were sourced from Sigma-Aldrich (Vienna, Austria) and S3 Chemicals,

respectively.

GDC-Zr-5/5 (Ce $_{0.9}$ Gd $_{0.05}$ Zr $_{0.05}$ O $_{1.975}$ ) was synthesized via a Pechinitype sol-gel method [21]. Stoichiometric amounts of Ce(NO $_3$ ) $_3$ ·6H $_2$ O, Gd (NO $_3$ ) $_3$ ·6H $_2$ O, and ZrOCl $_2$ ·8H $_2$ O (Alfa Aesar), citric acid monohydrate (C $_6$ H $_8$ O $_7$ ·H $_2$ O, VWR Chemicals), and ethylene glycol (C $_2$ H $_6$ O $_2$ , Thermo Scientific) were mixed in a 1:2 molar ratio of total metal ions to citric acid. The solution was heated at 80 °C to form a viscous gel, dried at 120 °C, and calcined at 800 °C for 2 h in air. The resulting powder was uniaxially pressed into bars (40  $\times$  4  $\times$  4 mm $^3$ ) and pellets (10 mm diameter  $\times$  1 mm thickness).

Samples were sintered in air as specified in the text in the high-temperature furnace HTF 18/08 from Carbolite Gero Ltd. (Hope, England).

Exposure tests were performed using the high-temperature furnace model 121212WM of Thermal Technology Inc. (Concord, United States of America).

#### 2.2. Characterization methods

The untreated pellet surfaces as well as cross-sections of the pellets, which were embedded in epoxy, ground and polished were analyzed by scanning electron microscopy (SEM) using a GeminiSEM 450 (Carl Zeiss Microscopy Deutschland GmbH, Oberkochen, Germany) equipped with an energy dispersive X-ray spectroscopy (EDS) detector Ultim® Max 170 (Oxford Instruments plc, Abingdon, UK).

Phase composition was analyzed by x-ray diffraction (XRD) using a Bruker D4 Endeavor diffractometer with Cu-K $\alpha$  radiation ( $\lambda=1.5406$  Å).

Vaporisation studies on GDC-10, GDC-Zr-5/5, and pure  $CeO_2$  and  $Gd_2O_3$  were performed using a Finnigan MAT 271 (Finnigan MAT, Bremen, Germany) 90 deg magnetic sector field mass spectrometer coupled with a Knudsen cell. To prevent reactions between the Knudsen cell and the samples, an iridium cell was used. The orifice in the lid of the cell had a diameter of 0.3 mm. The cell itself was placed in a molybdenum container, which had a hole at the bottom for temperature measurement, using an optical pyrometer. Experiments were conducted between 1300 °C and 1650 °C under high vacuum. Ion intensities of evaporated species (e.g.,  $CeO_2(g)$ , GdO(g), and Ce(g)) were recorded using a continuous dynode multiplier linked to an ion counter. Ionization of the species in the vapour phase was achieved by applying an electron energy of 70 eV and an emission current of 0.2 mA. Polythermal measurements were performed on at least three samples per materials to verify reproducibility of the results.

The thermodynamic activity of  ${\rm CeO_2}$  in GDC-10 and GDC-Zr-5/5 was determined according to the thermodynamic relationship as follows:

$$a(CeO_2) = \frac{p(CeO_2)}{p_0(CeO_2)} = \frac{I(CeO_2)}{I_0(CeO_2)} \tag{1} \label{eq:access}$$

where p,  $p_0$  and I,  $I_0$  are partial pressures of  $CeO_2$  and ion intensities of  $CeO_2^+$  ion, respectively, over the investigated material and saturated pressure over pure  $CeO_2$ .

A pushrod dilatometer (TA instruments, DIL 802 with SiC furnace) was used to measure chemical expansion/contraction during redox reaction. For this purpose, temperature-dependent length variations  $\varepsilon$ , based on the length variation  $\Delta l$  calculated from the sample length of the reduced  $L_{CeO2-\delta}(T)$  and oxidised state  $L_{CeO2}(T)$ , were measured and expansion coefficient  $\alpha$  was calculated as follows:

$$\varepsilon = \frac{\Delta l}{L} = \frac{(L_{CeO2-\delta}(T) - L_{CeO2}(T))}{L_{CeO2}(T)}$$
 (2)

$$\alpha = \frac{1}{L} \cdot \left( \frac{\partial l}{\partial T} \right)_{p} \tag{3}$$

Besides the variation of temperature, the atmospheres were changed between ambient air and low pressure to enable an oxygen uptake and

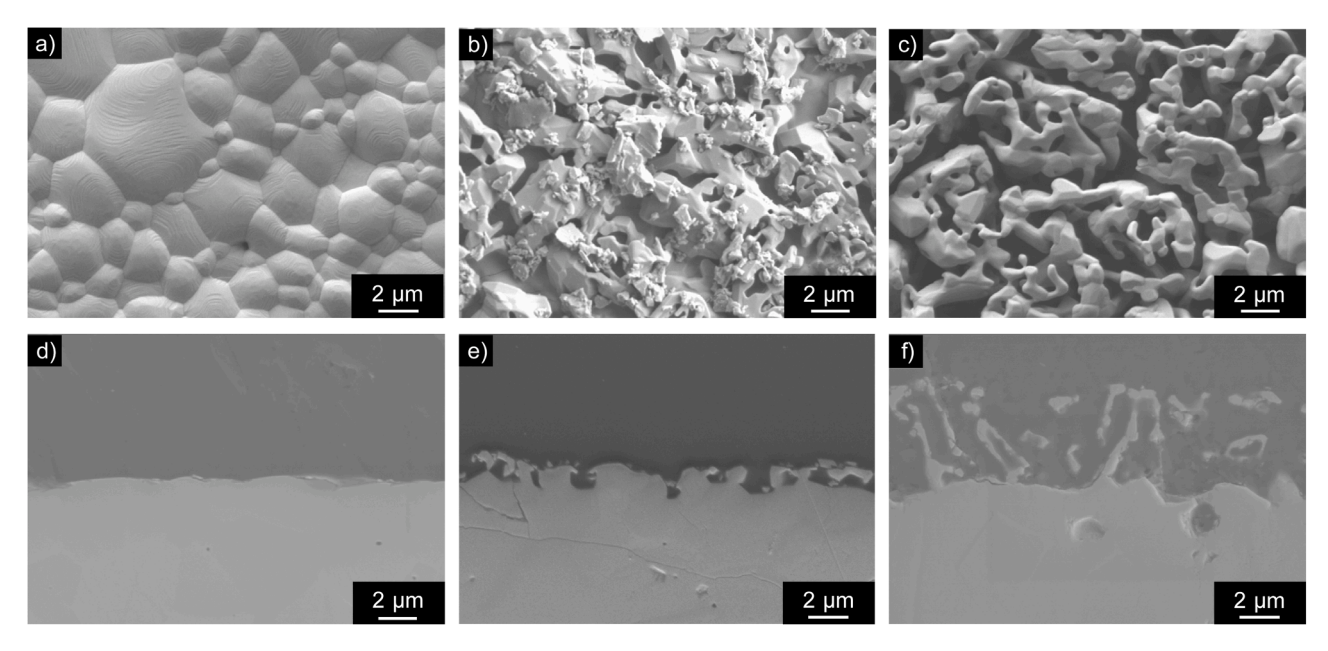


Fig. 1. Secondary electron (SE) images of the surface a)-c) and cross sections d)-f) of sintered GDC-10 pellet after different exposure times to vacuum at 1400 °C of initial state [a) & d)], 2 h [b) & e)] & 10 h [c) & f)] with an expected partial pressure of  $pO_2 = 10^{-7}$  bar.

release step corresponding to a full redox reaction. For reduction low total pressure (2  $\times$   $10^{-5}$  mbar) was reached by a turbo pump (Oerlikon Leybold vacuum). The turbo pump was working permanently over the whole experiment. The sample bars employed were placed on  $Al_2O_3$  carriers coated with Pt-foil and fixed with a push rod.

These push rod transfers the length change of the sample bar to a displacement sensor. A sapphire bar of the same length was measured simultaneously for calibration purposes. The temperature during redox reaction was determined by thermocouples located beside the sample bar. Temperature was ramped to the target temperature of 1200 °C-1400 °C at a rate of 6 °C/min for reduction, maintained for 120 min for further isothermal reduction and then ramped down to 25 °C at the rate of 6 °C/min. Reduction extents ( $\delta$ , Eq. 4) can be calculated with the changes in mass  $\Delta$  meq using an analytical balance before and after experiment, sample mass m<sub>s</sub>, molar mass of O and CeO<sub>2</sub> (M<sub>O</sub>, M).

$$\delta = \frac{M \cdot \Delta meq}{M_{\odot} \cdot m}.$$
 (4)

For re-oxidation, another temperature ramping was performed under ambient air to determine chemical contractions. The mass change after re-oxidation is here also measured after the experiment by an analytical balance

For Raman spectroscopy, a diode laser (532 nm) was utilized as a monochromatic excitation source, and a spectrometer (Horiba, XploRA Plus) coupled with 10x-magnification confocal lens was utilized. All Raman spectra were collected with 1800 g/mm grating, 100 mm slit

width, and 4 s of exposure.

Additional surface profiling were performed on an IONTOF TOF-SIMS.5 NCS system using a 30 keV Bi\* primary ion beam (50  $\mu m \times 50$   $\mu m$  raster) and 1 keV O- sputtering (250  $\mu m \times 250$   $\mu m$  raster). Charge compensation was achieved using a low-energy electron flood gun and argon flooding (2  $\times$  10 $^{-6}$  mbar). Depth profiles were acquired in positive ion mode.

## 3. Results and discussion

## 3.1. Microstructural stability of gadolinium doped ceria

## 3.1.1. Morphological and structural observation

To investigate structure and morphology changes by heating under low oxygen environment, the samples were also analysed after exposure to vacuum and argon. The images of the surface and cross-sections of pellets sintered at 1650 °C for 2 h (a) and (d), compared to those exposed to vacuum (b), (c), (e), and (f) in Fig. 1, do not show the dense structure previously observed. GDC-10 after exposure demonstrates significantly higher porosity, particularly near the surfaces, where spongy surface zones extending over several micrometres are evident. Due to the low total pressure during cycling ( $p=2\times10^{-5}$  mbar) and the high vapor pressure of ceria [22] segregation and subsequent selective sublimation could possibly cause the formation of a very porous surface zone. In previous studies on redox characteristics of ceria the results suggest sublimation of ceria at high temperature above 1300 °C and low total

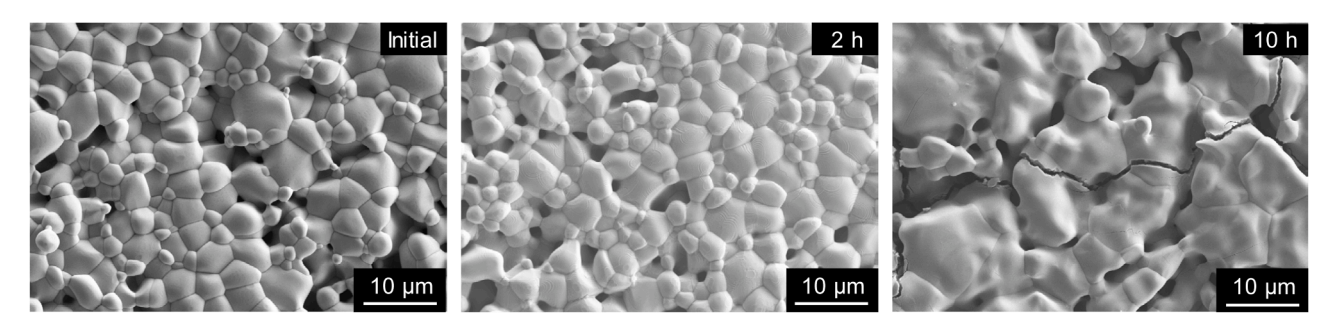


Fig. 2. SE-images of the surface of sintered GDC-10 pellets after different exposure times to 5 N argon at 1400  $^{\circ}$ C of 0, 2 & 10 h with a partial pressure of pO<sub>2</sub> =  $10^{-5}$  bar and flow of 200 l/h.

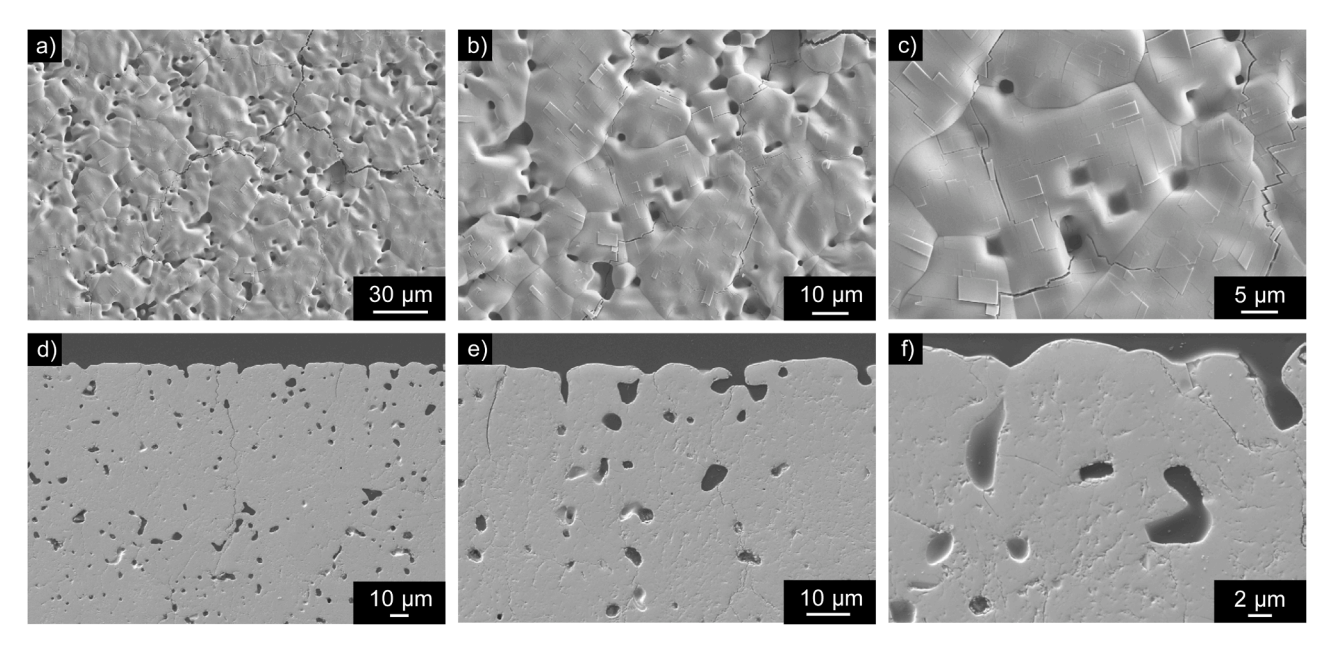


Fig. 3. SE-images of the surface a)-c) and cross section d)-f) of sintered GDC-10 pellet after exposure to 5 N argon at 1500  $^{\circ}$ C for 72 h with a pO<sub>2</sub> =  $10^{-5}$  bar and flow of 200 l/h.

pressure  $(10^{-5} \text{ mbar}) [17,23,24]$ .

The evaporation rate could be described by Hertz–Knudsen–Langmuir equation (Eq. 5) where  $d_{ni}/dt$  is the flux of particles hitting the surface in mol/s, A is the surface area,  $a_e$  and  $a_c$  are the coefficients of evaporation and condensation,  $p_{i,sat}$  is the saturated vapor pressure of element i,  $p_i$  is the actual partial pressure at the surface, R is the universal gas constant, T is the temperature in Kelvin, and  $M_i$  is the molar mass of the element. A detailed description and derivation of this equation is given in [25]:

$$\frac{d_{n_i}}{dt} = -A \frac{a_e p_{i,sat} - a_c p_i}{\sqrt{2\pi R M_i T}} \pi r^2$$
(5)

If the evaporation flux in vacuum is the same as in argon, the same surface phenomena would be expected. However, the results in Fig. 2 of samples previous sintered at  $1670~^{\circ}$ C for 6 h do not exhibit the same

surface changes at the same temperature. The samples thermally treated under argon for 2 hours do not show a porous surface layer like those treated under vacuum but only the formation of sintering steps due to increased cation mobility introduced by a lower oxygen partial pressure. With an extended exposure time of 10 hours, these surface changes become more pronounced. The higher mobility introduces a more smoothed surface and no longer visible sintering steps with a lot less clear grain boundaries on the surface. Besides that, also cracks are introduced both on the surface and in the bulk.

To further investigate the time parameter, the time was increased, too. However, even after 72 hours, no superficial segregation can be seen, under vacuum (Fig. 3). As well as the also for the 10 h 1400  $^{\circ}$ C observed cracks. Further the smoothening increased with larger grains, additionally a rectangular flaking and symmetrical pores can be seen on the surface. These formations were also observed in previous

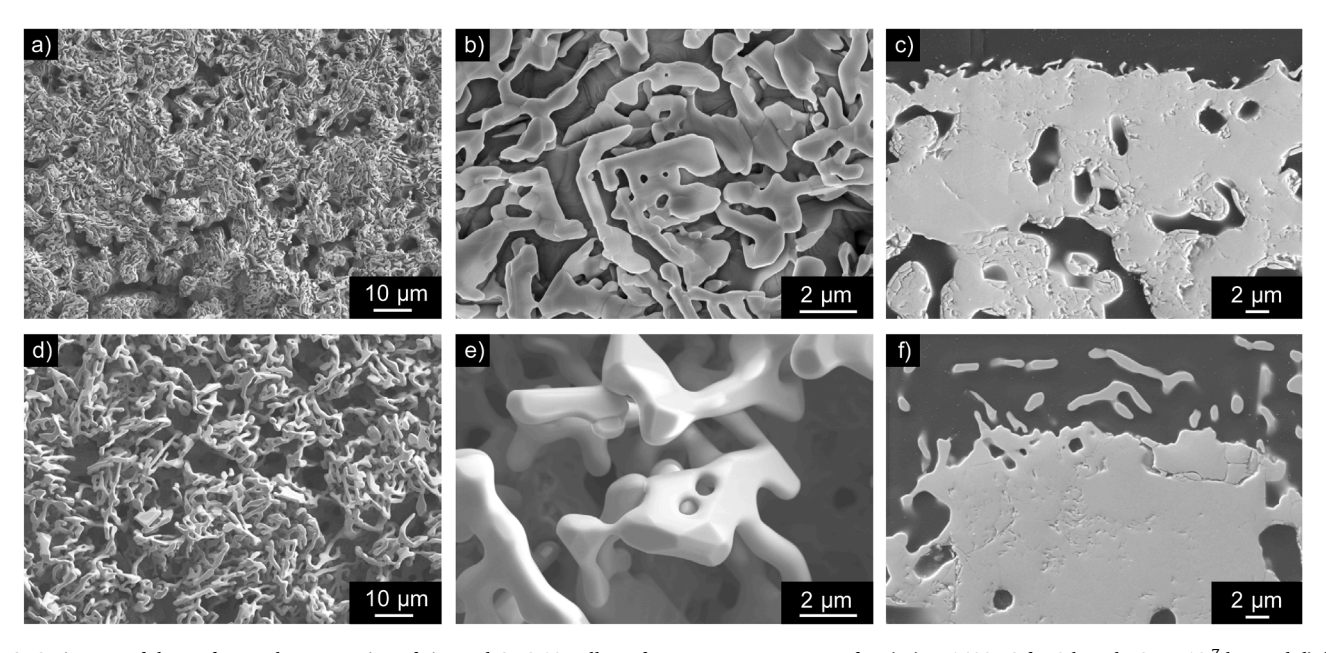


Fig. 4. SE-images of the surface and cross section of sintered GDC-10 pellets after exposure to vacuum for a)-c) at 1400 °C for 2 h and pO<sub>2</sub> =  $10^{-7}$  bar and d)-f) at 1500 °C for 6 h and pO<sub>2</sub> =  $10^{-7}$  bar.

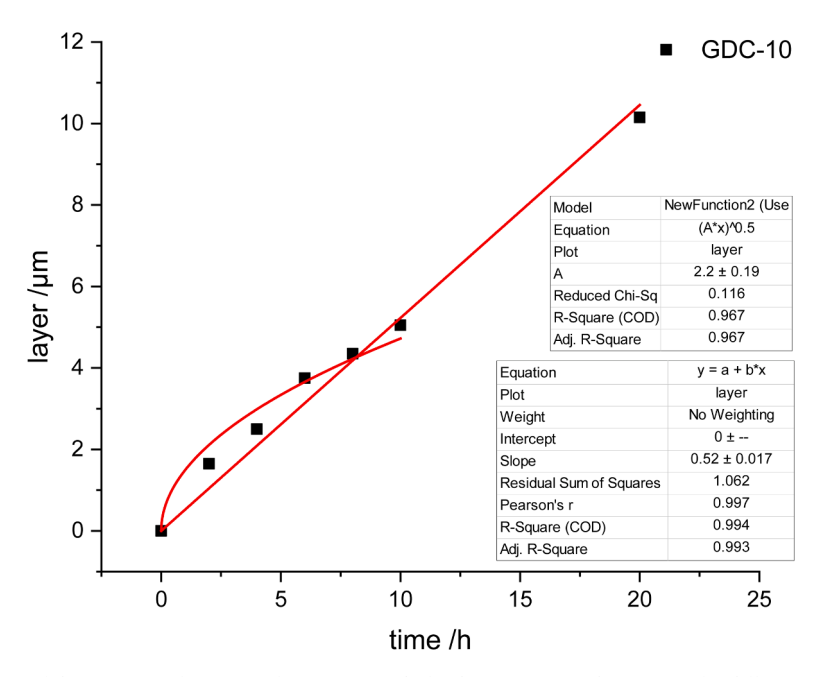


Fig. 5. Thickness of the porous surface zone of GDC-10 sample fired at 1400 °C under vacuum for different annealing times.

experiments by Knoblauch for undoped ceria [23] and as shown in the supplementary information (Figure S1). Additional exposures at  $1500\,^{\circ}\mathrm{C}$  in air for 72 hours showed no such changes. These findings exclude temperature and time as determining factors, suggesting that other variables play more significant roles in the observed phenomenon.

From this it can be concluded that the evaporation flux depends not only on the partial pressure of the cerium oxide but is also influenced by the gas transport in the environment. The difference in evaporation flux between vacuum and inert-gas flow can be explained by different pressure levels during both experiments [26]. Vacuum exposure tests were performed with a pressure level of  $10^{-5}$  mbar, which is several orders of magnitude lower than 1 bar of atmospheric pressure used for the 200 l/h argon-flow. The sublimation process in the system containing the compound in solid and gas phase is driven by the chemical potentials of both phases. The chemical potential rises with pressure and temperature with different rates for gases and solid materials [27]. As

the chemical potential of a gas increases more than the chemical potential of a solid, more energy is needed to sublimate the solid, i.e. for ambient pressure argon-flow we need to increase the temperature to sublimate the same amount of the substance as for vacuum. As the results show, the sublimation temperature under argon must be higher than  $1500\ ^{\circ}\text{C}.$ 

To gain a deeper understanding of the effects of vacuum exposure, additional testing has been conducted at 1500 °C. The comparison of both exposures in Fig. 4 reveals a significant increase in thickness of the porous layer, from around one micrometre to up to ten micrometres. The porous surface area also appeared thicker with more free spaces in between. In order to understand the influence of the dwell time in addition to the temperature, the GDC-10 samples were additionally treated at  $1400\,^{\circ}\mathrm{C}$  under vacuum for dwell times of 2 h, 4 h, 6 h, 8 h, 10 h and 20 h (see Figures S2–7). The thickness of the sublimation-related surface zone increases continuously with increasing exposure time. Fig. 5 shows the

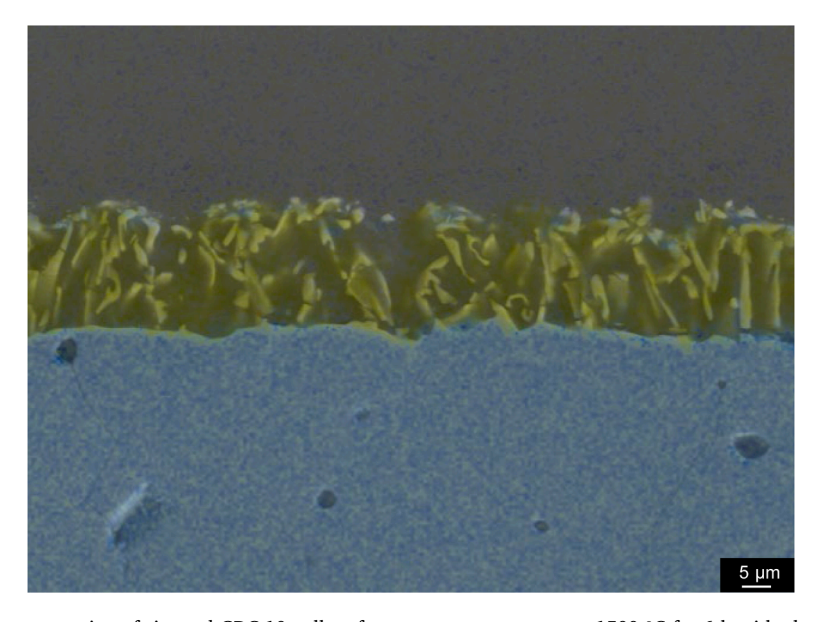


Fig. 6. SEM/EDS analyses of the cross section of sintered GDC-10 pellet after exposure to vacuum at 1500 °C for 6 h with elemental mappings of gadolinium in yellow and cerium in blue. (For interpretation of the references to color in this figure legend, the reader is referred to the web version of this article.).

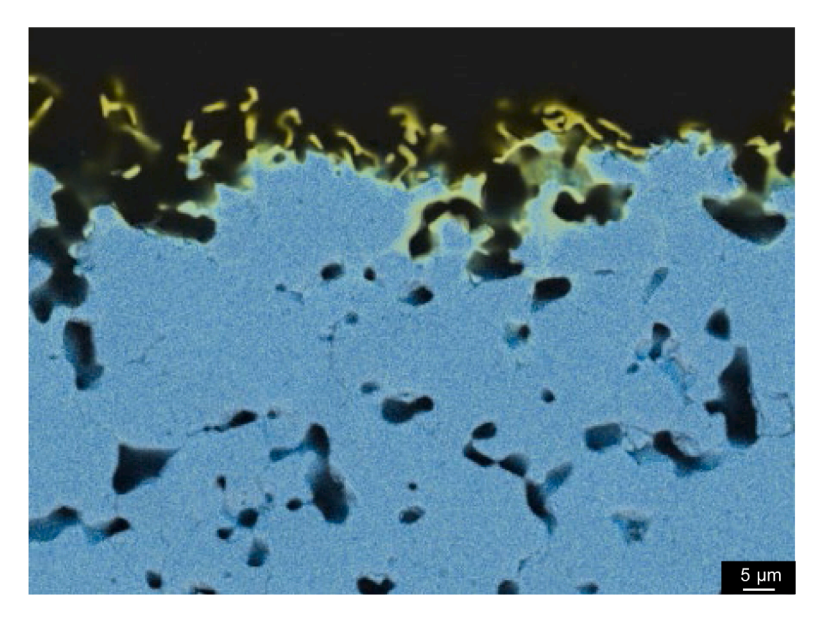


Fig. 7. SEM/EDS analyses of the cross section of sintered GDC-10 pellet after exposure to vacuum at 1500 °C for 6 h with elemental mappings of gadolinium in yellow and cerium in blue. (For interpretation of the references to color in this figure legend, the reader is referred to the web version of this article.).

depths (l) determined by SEM after the corresponding annealing time under vacuum. The growth of the evaporation zone initially appears to follow a parabolic time law. After a longer time > 5 h, the growth changes from parabolic to linear growth (adjusted with the software OriginLab Inc., USA using this fitting equation  $l \approx \sqrt{(A \bullet t)}$  and  $l \approx A^* t$ ). Diffusion determines the rate in the initial phase, while only surface exchange determines the rate as the process progresses. The different behaviour could be explained by the fact that evaporation occurs at the bulk at the beginning and later mainly in the porous surface layer.

An EDS analysis (Fig. 6) of the 1400 °C, 10 hours exposure revealed an enrichment of gadolinium in the porous surface area and a depletion of ceria. In addition, an increase of the exposure conditions to 1500 °C for 6 hours of a more porous sample sintered at 1670 °C for 6 h showed a less homogenous surface area along with contamination of tungsten and silicon on the surface area. The silicon contamination can be attributed to the heating elements used in the sintering oven, while the tungsten contamination is due to the tungsten heating elements in the vacuum oven. Since contamination levels were already high, extended exposure

times showed no additional gains. Fig. 7 shows the Ce/Gd distribution within the SEM images, indicating that the Gadolinium enrichment is not only observed on the surface but also occurs within the porous area close to the surface. Time-of-flight secondary ion mass spectrometry (TOF-SIMS) measurements were conducted on this cross-section and confirmed the enrichment of Gadolinium in the surface, while the enrichment in the pores connected to the surface were undetectable due to a to high surface roughness.

The absence of gadolinium enrichment and ceria depletion on the pore surfaces within the bulk in suggests that the pores may be sealed without connection to the surface, containing a normal atmosphere with oxygen, which inhibits ceria evaporation. This hypothesis would mean that the normal atmosphere introduced during the manufacturing is still present within the pores throughout the exposure.

Systematic SIMS experiments were initiated to monitor and quantify the enrichment. Initial attempts using the sample in Fig. 7 and scanning it with a sputtering depth in the nanometre range were unsuccessful due to the high porosity of the sample.

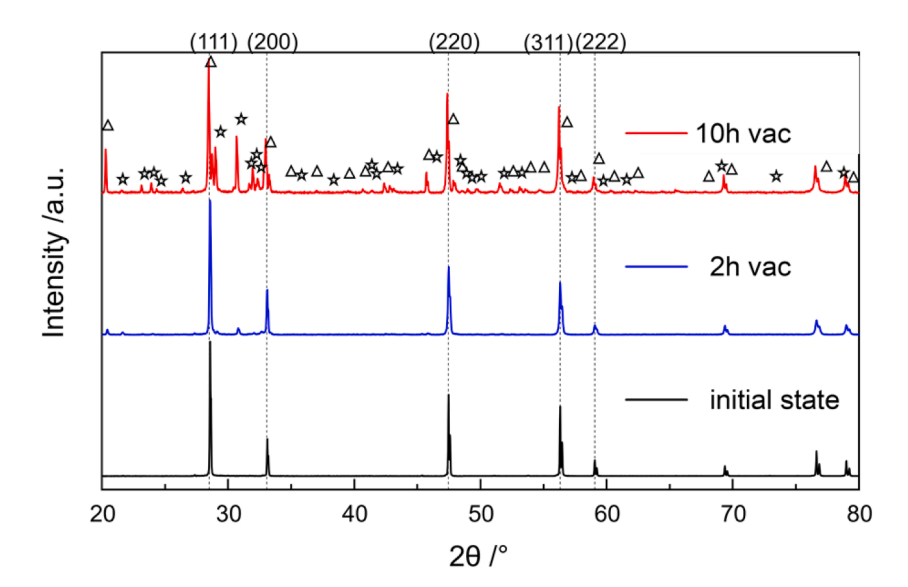


Fig. 8. XRD pattern of GDC-10 after heat treatment at 1650 °C (initial state) and vacuum exposure (pO<sub>2</sub>=6  $\times$  10<sup>-7</sup> mbar) for 2 h and 10 h. Reference Gd<sub>2</sub>O<sub>3</sub>, PDF 12–0797 marked with triangles and Gd<sub>2</sub>SiO<sub>5</sub>, PDF 40-0287 marked with asterisks.

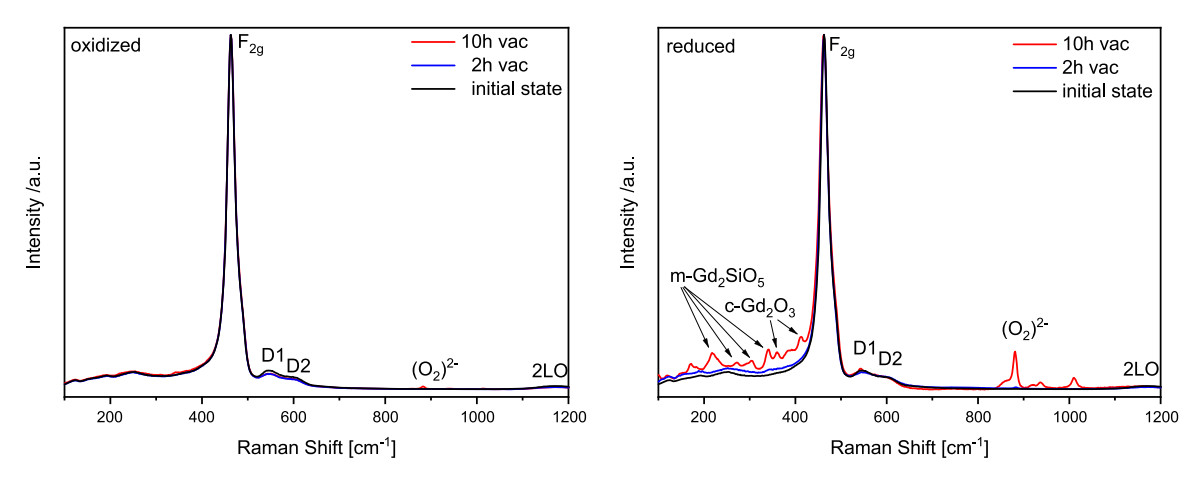


Fig. 9. Comparison of Raman spectra of oxidized and reduced GDC-10 before and after exposure to vacuum at 1400 °C for 2 h and 10 h.

The obtained isomer peaks were too broad, and quantification was discarded because of a non-matching isotope pattern of gadolinium to the natural distribution. However, the enrichment of gadolinium could be confirmed.

## 3.1.2. Crystallographic phase evaluation

To support the preceding results of the SEM and EDS and the assumption that the doping element concentration at the surface changes, further analyses of the samples were carried out with XRD to obtain more information about the phases and compositions involved. Thus, pellet samples were examined after heat treatment at 1650 °C before cycling (Fig. 8, 0 h). The XRD patterns shows sharp reflections with the expected fluorite-type crystal structure of doped cerium oxides. The main XRD reflections are only slightly shifted due to the dopantinduced expansion of the crystal lattice. For further investigation the lattice constants of GDC-10 were calculated by the Rietveld method based on the XRD profile fitting. The fitted lattice constant belongs to a= 5.413 Å which is close to the calculated lattice constant a = 5.418 Å given by the equation of Hong and Virkar [28]. Besides pellet samples before cycling, pellets exposed to 1400 °C under vacuum were analysed using XRD, as the SEM and EDS results suggest that selective sublimation has taken place. This sublimation and dopant enrichment could lead to a

change in the crystal structure at the pellet surface. The XRD results of altered pellets in Fig. 8 (2 h,10 h) show reflections of the CaF $_2$  structure as seen before and additional smaller reflections which increase with increasing exposure time. The less intense reflections could be identified to be a cubic gadolinium oxide (Gd $_2$ O $_3$ , PDF 12-0797) and a monoclinic gadolinium silicate phase (Gd $_2$ SiO $_5$ , PDF 40-0287). It can be assumed that selective sublimation leads to an enrichment of gadolinium leading to the formation of Gd $_2$ O $_3$ . The Gd $_2$ SiO $_5$  formation is probably due to contamination with Silicon from the SiC furnace.

Raman Spectroscopy was performed for further insights about the structural and cation-ordering features in the oxidized and reduced state. Raman spectroscopy is primarily sensitive to oxygen cation vibrations and is an excellent method for local disorder. Normalized Raman spectra of reduced and oxidised GDC-10 are shown in Fig. 9.  $F_{2g}$  Raman mode at around 460 cm<sup>-1</sup> is a dominant Raman reflection for the cubic calcium-fluorite-structured materials, corresponding to the symmetrical stretching of Ce-8O vibrational unit for ceria [29–31]. The characteristics of the  $F_{2g}$  mode is well investigated for ceria-based materials in view of reflection position [29,30] and full-width at half maximum [31]. The reflection position is linearly correlated to the lattice constant, so the reflection is shifted to lower frequency of 462 cm<sup>-1</sup> (CeO2  $\tilde{\nu} = 466$  cm<sup>-1</sup> [32]) in the case of the Gd-doped CeO<sub>2</sub> sample [33,

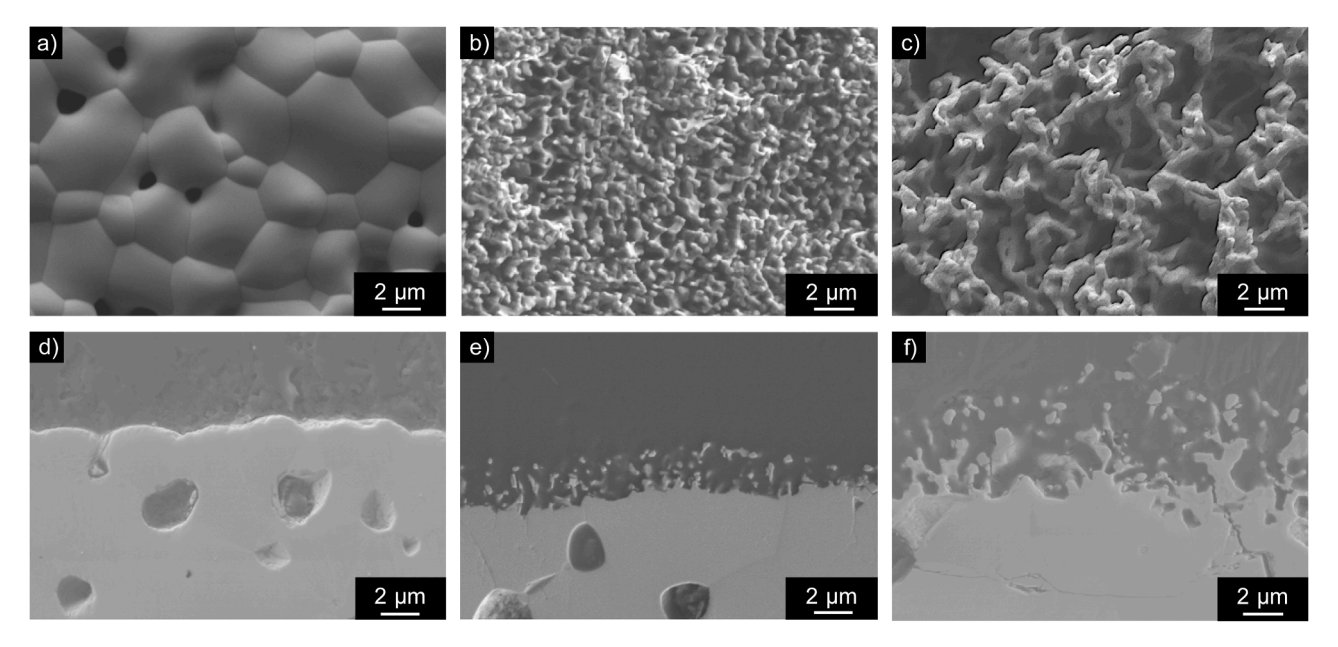


**Fig. 10.** Secondary electron SE-images of the surface a)-c) and cross sections d)-f) of sintered GDC-Zr-5/5 pellet after different exposure times to vacuum at 1400 °C of initial state [a) & d)], 2 [b) & e)] & 10 h [c) & f)] with a partial pressure of pO<sub>2</sub> =  $10^{-7}$  bar.

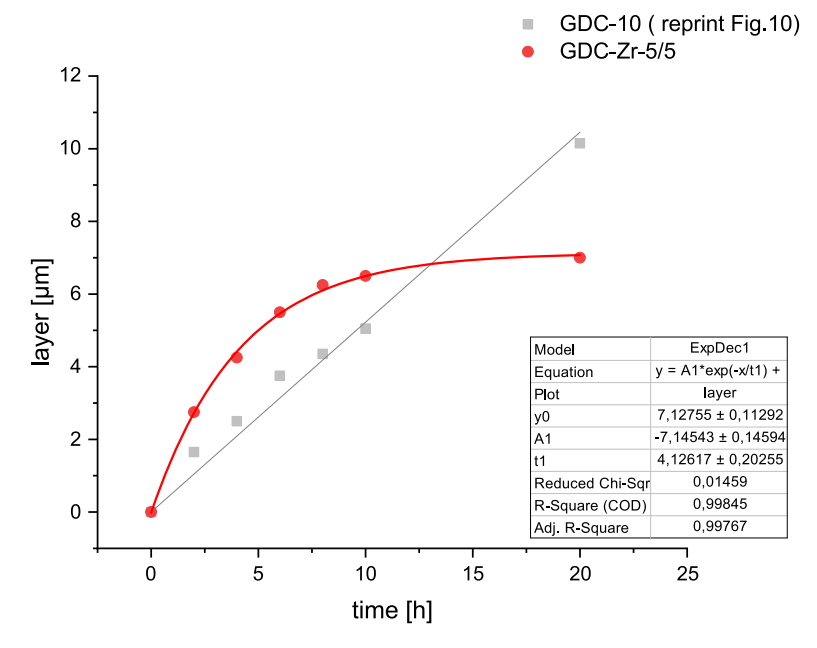


Fig. 11. Thickness of the porous surface zone of GDC-10 in black and GDC-Zr-5/5 sample in red fired at 1400 °C under vacuum for different annealing times. (For interpretation of the references to color in this figure legend, the reader is referred to the web version of this article.).

34]. Based on the  $F_{2g}$  Raman mode, the sintered pellet (0 h) were in cubic fluorite structure and there was no sign of an additional phase. Only second order features at lower frequency (264 cm<sup>-1</sup> and 366 cm<sup>-1</sup>) [35] and defect-induced disorder bands at 500-650 cm<sup>-1</sup> are shown as low intensity bands shoulder of the  $F_{2g}$  Raman mode.  $D_1$  band at 530-550 cm<sup>-1</sup> correspond to oxygen vacancy-induced defects resulting from the different oxidation states of  $Gd^{3+}$  compared with  $Ce^{4+}((2Gd'_{Ce}:V_O^*)^x$  and  $(Gd'_{Ce}:V_O^*)$  complexes)  $D_2$  band at 600 cm<sup>-1</sup> belongs to  $GdO_8$ -type complex defects due to the different ionic radius of  $Gd^{3+}$  (1.053 Å) compared to that of  $Ce^{4+}$  (0.97 Å) [31,36].

In the reduced state especially after exposure time of 10 h under vacuum several new bands appear. These additional bands are visible in contrast to the reoxidized sample due to the fact that the Raman intensity of the  $F_{2g}$  Raman mode is reduced. In reduced samples, the Raman intensity decreases as a direct response to the decrease in the oxygen content of the sample and the resulting changes in the optical properties of the surface, such as absorption and reflection [37]. One of

the new bands located between 800 and 900 cm $^{-1}$  fits to  $\nu(O=O)$  stretching vibrations of peroxo species which could be formed upon oxygen adsorption on reduced ceria [32]. Furthermore we observed some true Raman bands of the sesquioxides which are featured bands at about 330 to 420 cm $^{-1}$  (the Fg+ Ag mode) [38] and bands between 217 and 340 cm $^{-1}$  which fit well to bands observed for monoclinic Gd<sub>2</sub>SiO<sub>5</sub> [39]. Thus, the presence of a c-Gd<sub>2</sub>O<sub>3</sub> phase and m-Gd<sub>2</sub>SiO<sub>5</sub>, which was also previously detected with XRD, can also be confirmed with Raman.

## $3.2. \ \textit{Microstructural stability of gadolinium/zirconium doped ceria}$

To better understand the factors influencing the selective sublimation observed with GDC-10, beside atmosphere variations different material compositions are also investigated. For influencing the diffusion, discussed as rate determining step for sublimation, co-doping with Zr was also analyzed. The additional  $Zr^{4+}$  could lead to phase stabilization by provoking pyrochlore ( $A_2B_2O_7$ ,  $A=Zr^{4+}$ ,  $B=Ce^{3+}$ ,  $Gd^{3+}$ )

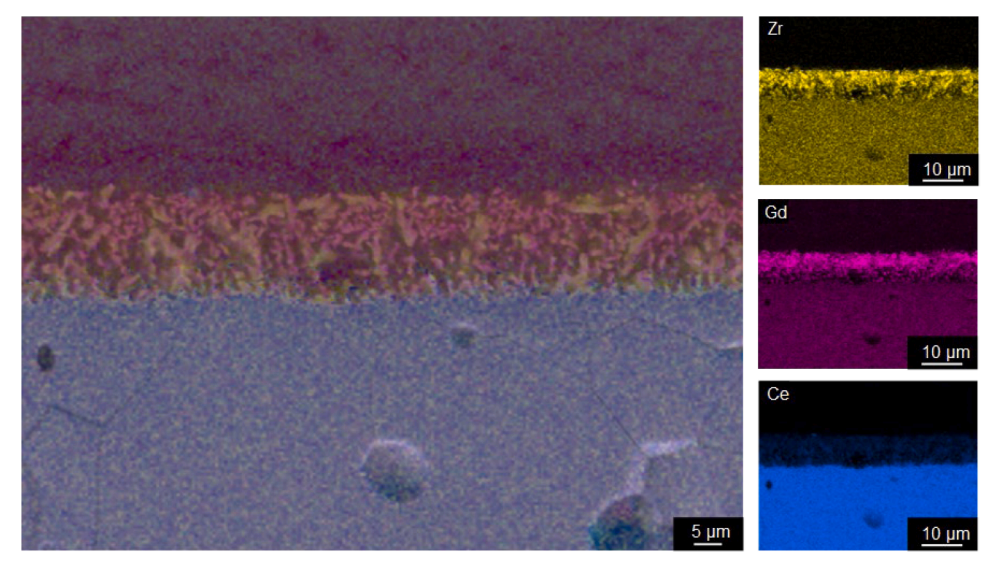


Fig. 12. SEM/EDS analyses of the cross section of sintered GDC-Zr-5/5 pellet after exposure to vacuum at 1400 °C for 10 h.

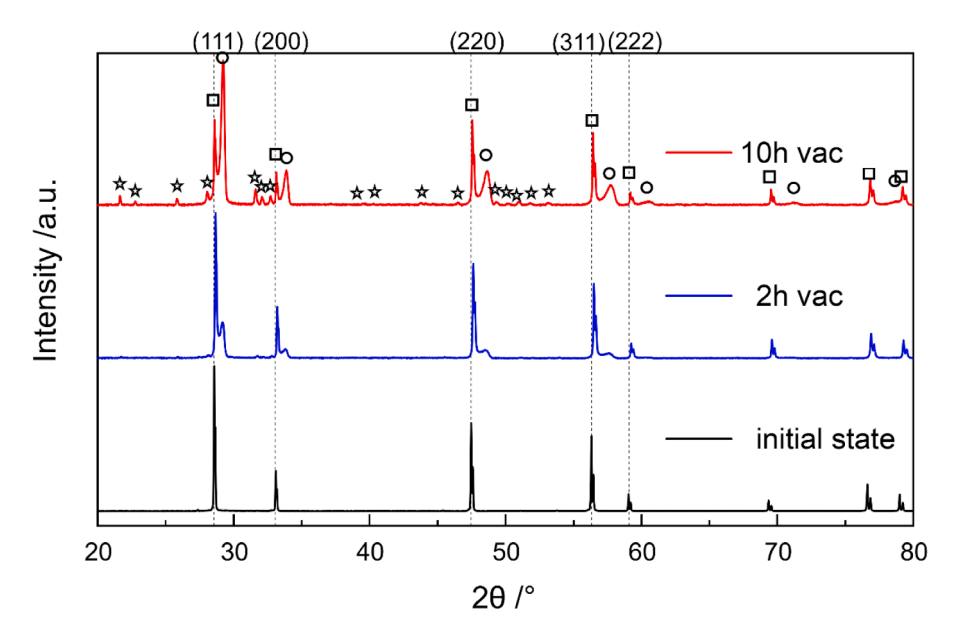


Fig. 13. XRD pattern of GDC-Zr-5/5 after heat treatment at 1650 °C (initial state) and vacuum exposure ( $pO_2=6 \times 10^{-7}$  bar) for 2 h and 10 h. Reference  $Gd_{4.67}(SiO_4)_3O$ , PDF 72-2070 marked with asterisks and CeO2, PDF 04-0593 marked with square for Gd-rich and marked with circle for Zr-rich.

formation due its small ionic radius in comparison to  $Ce^{3+}$  and  $Gd^{3+}$  [40, 41].

## 3.2.1. Morphological and structural observation

To investigate structure and morphology changes due to doping with  ${\rm Zr}^{4+}$  the same exposure test as with GDC-10 are performed. The images of the surface and of the cross-sections of the pellets after sintering (0 h) in Fig. 10 do not show the dense structure observed before for GDC-10. GDC-Zr-5/5 shows a few pores despite the high sintering temperature, although there is a closed porosity overall. After exposure porosity increases, especially close to the surfaces, where spongy surface zones extending over several micrometre depth appear. Due to the low total pressure and the high vapour pressure of CeO<sub>2</sub> compared to Gd<sub>2</sub>O<sub>3</sub> and ZrO<sub>2</sub> [22], segregation by selective sublimation is also possible here. Compared to GDC-10, the porous surface structure here is more delicate.

For investigating the influence of the dwell time and for comparison to GDC-10, the GDC-Zr-5/5 samples were additionally treated at 1400 °C under vacuum for dwell times of 2 h, 4 h, 6 h, 8 h, 10 h and 20 h (Figures S8-13), too. The thickness of the sublimation-related surface zone increases also continuously with increasing exposure time. Fig. 11 shows the depths (1) determined by SEM after the corresponding annealing time under vacuum. The depths were fitted with an exponential function (fitted with software OriginLab Inc., USA using this fit equation expDec1 y = A1\*exp(-x/t1) + y0). Compared to GDC-10, sublimation seems to be limited by another mechanism. No initial parabolic growth and no linear increase in the sublimation zone after prolonged exposure is observed here. For GDC-Zr-5/5, it appears that the kinetics are much faster but the further sublimation slows down with increasing exposure. Since this kinetics do not follow a parabolic time law, a pure diffusion barrier is unlikely. The additionally introduced Zr<sup>4+</sup> could decrease the sublimation by phase stabilisation. Due to its small ionic radius, Zr<sup>4+</sup> could favour a pyrochlore configuration [40] which appears to increase the bond strength to  $Gd^{3+}/Ce^{3+}$  and thereby the lattice energy

An EDS analysis (Fig. 12) of the 1400  $^{\circ}$ C, 10 h exposure revealed an enrichment of gadolinium and zirconium in the porous surface area as expected. The layered image shows the Gd/Zr distribution in the sublimation area and reveals a phase separation in Gd rich and Zr rich zones. The Gd-rich zones appear thicker than the Zr-rich regions. The difference in thickness could be attributed to a different diffusion rate of the cerium ions. Due to the larger ionic radius of  $Ce^{3+}$  (CN 8, 114.3 pm)

compared to  $\mathrm{Gd^{3+}}(\mathrm{CN~8,105.3~pm})$ , pyrochlore formation between  $\mathrm{Zr^{4+}}$  and  $\mathrm{Ce^{3+}}$  is favoured [41,42]. Due to the higher amount of disorder in the pyrochlores with small A cations and large B cations, the  $\mathrm{Ce^{4+}}$  ions can diffuse more easily here, which leads to a faster depletion of the Zr-rich surface regions. This would confirm the previous observations that the  $\mathrm{Ce^{4+}}$  ions diffuse and sublimate faster in the initial time when  $\mathrm{Zr^{4+}}$  ions are present. After prolonged aging, sublimation could slow down due to depletion of  $\mathrm{Ce^{4+}}$  and preferential pyrochlore formation in the Zr-rich regions. In order to show an effect on the growth curve of the sublimation zone, the Zr-rich phase would have to predominate over the Gd-rich phase and this seems to be the case according to EDS.

## 3.2.2. Crystallographic phase evaluation

For a more in-depth examination of the surface zone and to support the preceding findings of the SEM and EDS, the samples were analyzed by XRD. Thus, pellet samples were examined after heat treatment at 1650 °C before exposure (Fig. 13, 0 h). The XRD pattern shows reflections of the expected fluorite-type crystal structure of doped cerium oxides with a slightly shift due to the dopant-induced expansion of the crystal lattice. For detailed investigation the lattice constant of GDC-Zr-5/5 was calculated by the Rietveld method based on the XRD profile fitting. The fitted lattice constant belongs to  $a = 5.403 \,\text{Å}$  which is smaller in comparison to GDC-10 due to smaller Ionic radius of Zr<sup>4+</sup>[41] but close to the calculated lattice constant  $a = 5.400 \,\text{Å}$  given by the equation of Hong and Virkar [28].

Beside the initial state, pellets exposed to 1400  $^{\circ}\text{C}$  under vacuum were analysed using XRD. The selective sublimation observed by SEM and EDS could lead to a change in the crystal structure at the pellet surface. The XRD results of altered pellets in Fig. 13 (2 h,10 h) show, reflections of the CaF2 structure as seen before and additional smaller reflections which increase with increasing exposure time. The smaller reflections marked by stars which appear after long exposure times could be identified to be a cubic gadolinium silicate phase  $(Gd_{4.67}(SiO_4)_3O, PDF 72-2070)$ . The  $Gd_{4.67}(SiO_4)_3O$  formation is probably due to contamination with Si from the SiC furnace. Furthermore GDC-Zr-5/5 shows a splitting of the main cubic phase after 2 h exposure in vacuum. It can be assumed that selective sublimation separates the original single phase into a cubic Zr-rich phase and a Gd-rich phase. For detailed investigation the lattice constants of these new phases are calculated by the Rietveld method based on the XRD profile fitting. The lattice constant of the Zr-rich phase belongs to a<sub>1</sub>=5.303 Å and the Gd-

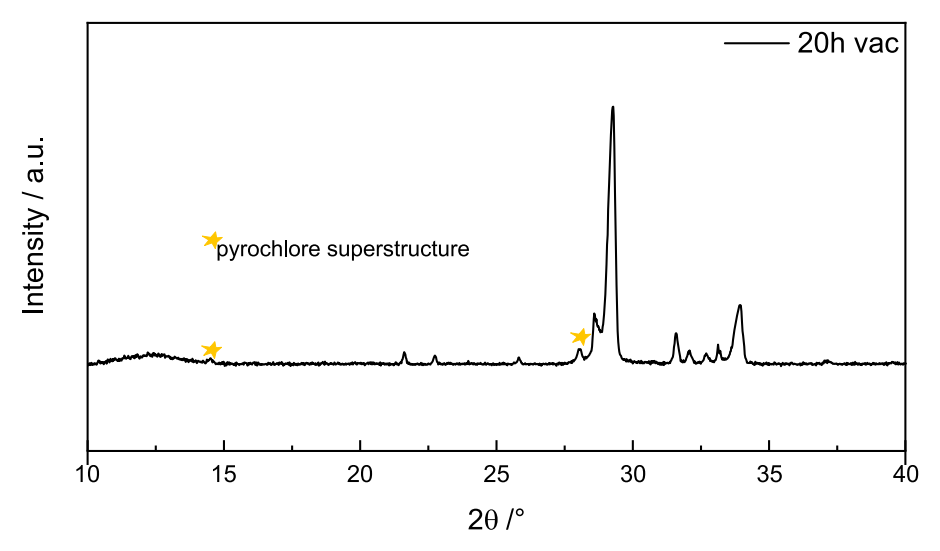


Fig. 14. XRD pattern of GDC-Zr-5/5 after vacuum exposure (pO<sub>2</sub>= $6 \times 10^{-7}$  bar) for 20 h. (asterisks correspond to the superstructure reflections).

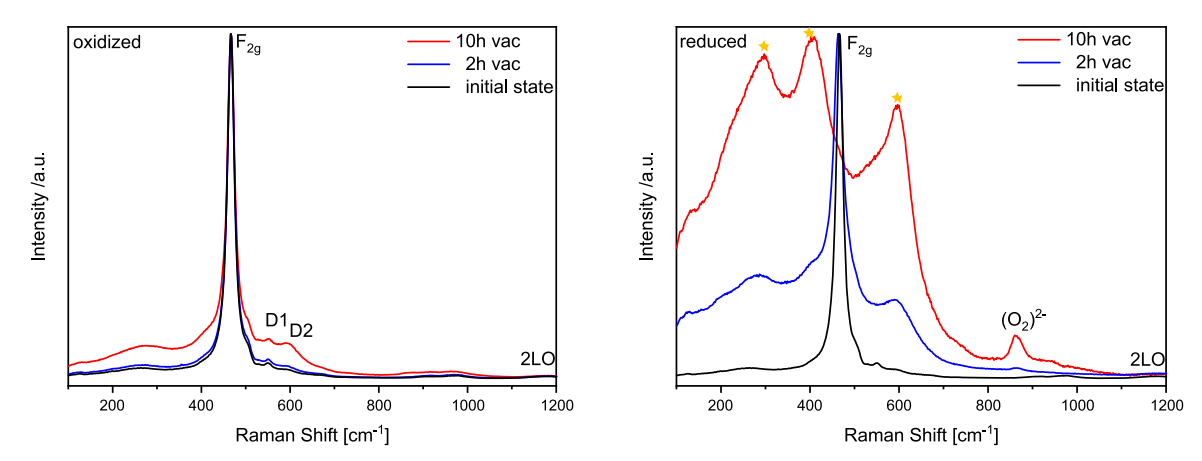


Fig. 15. Comparison of Raman spectra of oxidized and reduced GDC-Zr-5/5 before and after exposure to vacuum at 1400 °C for 2 h and 10 h.

rich phase to  $a_2=5.403~\text{Å}$  as the initial state. In the case of higher Zr concentration pyrochlore configurations are possible [40]. Distinguishing a fluorite structure from a pyrochlore structure using XRD is not easy because many reflections are identical, but there are superstructure reflections attributable to the Fd $\overline{3}$ m symmetry of a typical pyrochlore lattice that can provide a hint. Due to the fact that the concentration of the Zr-rich phase increases with longer aging times, the superstructure reflections are most clearly observable after 20 hours of aging.

Fig. 14 shows the XRD pattern of GDC-Zr-5/5 after exposure to vacuum for 20 h. As expected, the Zr-rich phase increases. In view of the assumption that a pyrochlore configuration could be present, a detailed investigation was made for corresponding superstructure reflections at small theta angles. Mandal et al. refer to two small superstructure reflections at approx. 14.5  $^{\circ}$  and 27.6  $^{\circ}$  as indicators for the presence of crystalline pyrochlore phases (Fd3m) with correspondingly reduced symmetry of fluorite structure (Fm3m) [43]. The result shows these corresponding superstructure reflections which indicate a pyrochlore configuration.

Raman spectroscopic studies were performed to gain further insight into the structural and cationic ordering features of the phases formed on the surface. Raman spectroscopy is sensitive to oxygen cation vibrations and is an excellent sensor for local disorder. Thus, Raman spectroscopic studies can provide information to distinguish closely related structures such as fluorite and pyrochlore. Therefore, Raman

spectroscopy has been performed on reoxidized and reduced samples to examine the presence (leading to the pyrochlore structure) or absence (leading to the defect fluorite structure) of ordering in the samples. Fig. 15 shows the Raman spectra of the reoxidized and reduced state after 0 h, 2 h and 10 h exposure to 1400  $^{\circ}$ C and vacuum.

The oxidized state of GDC-Zr-5/5 shows the F2g Raman mode, characteristic for cubic fluorite structure, second order features at lower frequency (264 cm $^{-1}$  and 366 cm $^{-1}$ ) [35] and defect-induced disorder bands at 500-650 cm $^{-1}$  as shown before for GDC-10. As with GDC-10, a clear decrease in the main  $F_{2g}$  band can be observed in the reduced state with increasing aging time, which makes changes on the surface visible. The main band mainly gives way to three new bands around 290, 405 and 595 cm<sup>-1</sup>, which show a high similarity to the Raman spectrum of Mandal et al. for a pyrochlore structure of the composition Gd<sub>0.5</sub>Ce<sub>1.5</sub>Zr<sub>2</sub>O<sub>7</sub>. The fact that the presumed pyrochlore structure is only visible in the reduced state can again be partly explained by the decrease in the F2g main band in the reduced state, but the literature also reports that (Gd-Ce-Zr) pyrochlores are sometimes only metastable, depending on their exact composition, and can transform back into the fluorite lattice when exposed to air by heating at high temperatures (e.g. 1400 °C) [44]. In addition to the pyrochlore bands, an additional band at approx. 865 cm<sup>-1</sup> can again be observed, which is due to the  $\nu$ (O=O) stretching vibration of the peroxo groups adsorbing on the sample surface of the reduced sample. To summarize, the presumed pyrochlore structure forms on the sample surface increase with exposure time. Since a pyrochlore configuration is favored by small Zr<sup>4+</sup> ions and larger Ce<sup>3+</sup>

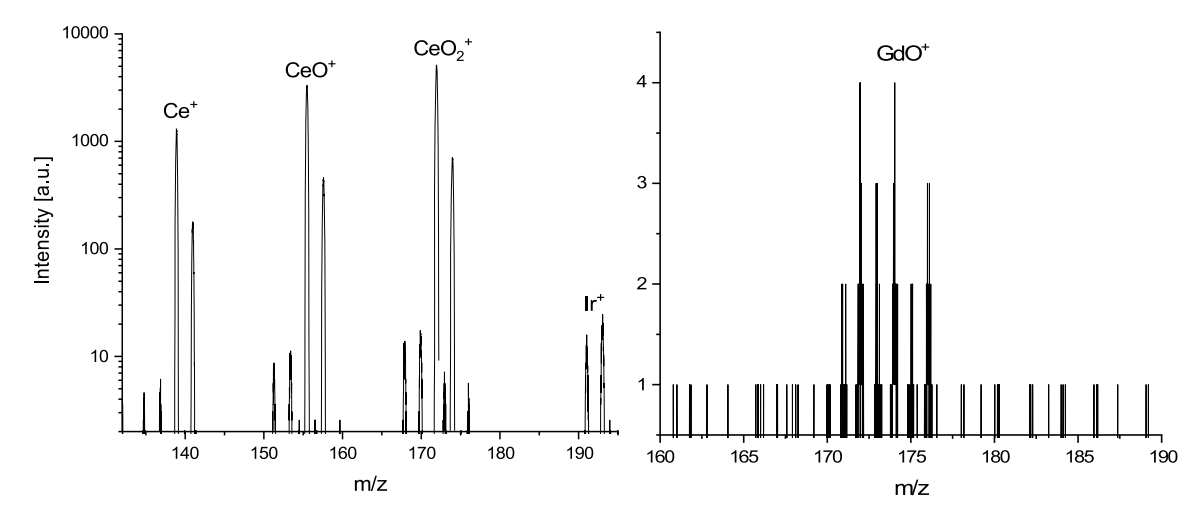


Fig. 16. Mass spectra of GDC-10 recorded at 1645 °C (left) and Gd<sub>2</sub>O<sub>3</sub> at 1800 °C (right).

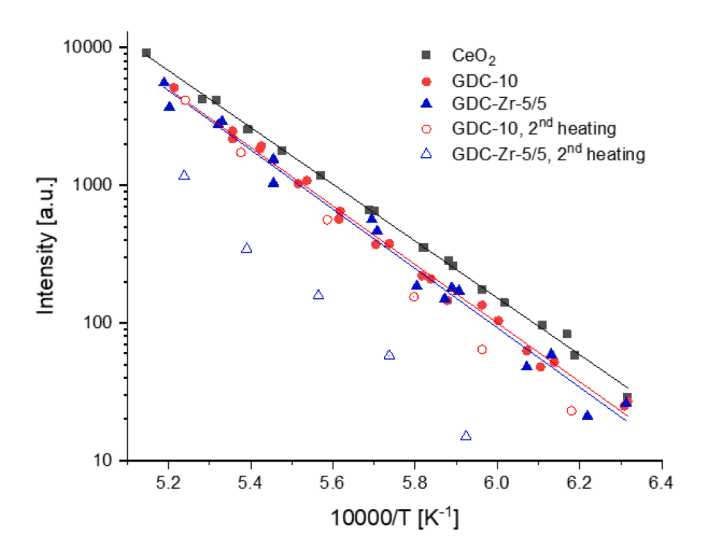


Fig. 17. Ion intensities of  $^{140} \text{CeO}_2^+$  over CeO2, GDC-10, and GDC-Zr-5/5 at 1300-1650  $^{\circ}\text{C}.$ 

ions [42], a decrease in  $Ce^{4+}$ ion concentration on the sample surface over time can be assumed.

## 3.3. Evaporation mechanism studies

Within the entire measured temperature range of 13,00-1650 °C, Ce $^+$ , CeO $^+$ , and CeO $_2^+$  ions were observed in the mass spectra of GDC-10 and GDC-Zr-5/5 (Fig. 16). The average ratio of the respective ion current intensities was about 26:65:100. While even Ir $^+$  from the Knudsen cell and the minor cerium isotopes (e.g. 0.2 %  $^{136}\text{Ce}$ , 0.3 %  $^{138}\text{Ce}$ , 0.1 %  $^{141}\text{Ce}$ , and 0.1 %  $^{144}\text{Ce}$ ) were clearly detectable over GDC-10 at 1645 °C, GdO $^+$ , the ion with the highest intensity, could only be detected with very low intensity at 1800 °C over pure Gd<sub>2</sub>O<sub>3</sub> (Fig. 16), which is in good agreement with investigations by Shugurov et al [18]. Zirconium containing species were not detectable over GDC-Zr-5/5 in the measured temperature range.

Since the  $\text{CeO}_2^+$  ion and in particular the isotope  $^{140}\text{CeO}_2^+$  (172 mass number) had the highest intensity in all measurements, it was selected for comparison of the  $\text{CeO}_2$  activity in the several samples.

Fig. 17 shows the measured ion intensities of  $^{140}\text{CeO}_2^+$  over pure  $^{140}\text{CeO}_2^+$  over gover gover gover gover gover gover gover gover than the intensities over pure  $^{140}\text{CeO}_2^+$  indicating that no pure  $^{140}\text{CeO}_2^+$  from incomplete reaction during synthesis was present in the doped materials. The difference between GDC-10 and GDC-Zr-5/5 lies in the measurement accuracy range. During the first heating, all materials showed acceptable reproducibility. However, during the second heating, the ion intensities

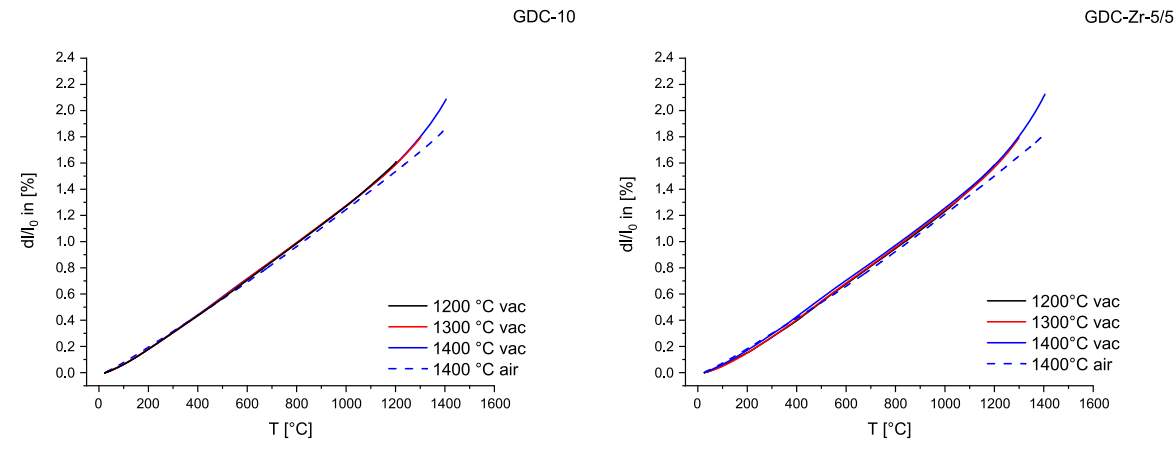


Fig. 18. Relative length change of GDC-10 and GDC-Zr-5/5 under air and vacuum (pO<sub>2</sub>= $6 \times 10^{-7}$  bar) as function of temperature.

Table 1

The linear coefficients of thermal expansion of GDC-10 compared to doped ceria in the literature.

Sample	CTE 100-1200 °C (K <sup>-1</sup> )
CeO <sub>2</sub> [23]	$14 \times 10^{-6} \pm 2 \times 10^{-8}$
$Ce_{0.9}La_{0.1}O_{1.95}$ [17]	$13\times 10^{-6}\pm 2\times 10^{-8}$
$Ce_{0.9}Yb_{0.1}O_{1.95}$ [17]	$13\times 10^{-6}\pm 1\times 10^{-8}$
$Ce_{0.9}Zr_{0.1}O_2$ [17]	$14.0\times 10^{-6}\pm 0.7\times 10^{-8}$
$Ce_{0.9}Gd_{0.1}O_{1.95}$ [44]	$13 \times 10^{-6}$ (613 °C)
$Ce_{0.9}Zr_{0.05}La_{0.05}O_{1.975}$ [17]	$14\times 10^{-6}\pm 1\times 10^{-8}$
$Ce_{0.9}Zr_{0.05}Yb_{0.05}O_{1.975}$ [17]	$14  imes 10^{-6} \pm 1  imes 10^{-8}$
GDC-10	$13  imes 10^{-6} \pm 1  imes 10^{-8}$
GDC-Zr-5/5	$13\times 10^{-6}\pm 2\times 10^{-8}$

measured over GDC-10 and GDC-Zr-5/5 decreased significantly with a steeper decrease for GDC-Zr-5/5 than for GDC-10. Moreover, the extent of the decrease was not well reproducible as initial measurements on all samples at about 1350-1400  $^{\circ}\text{C}$  revealed. Therefore, only one sample of each material was measured over the entire temperature range as an example. Consequently, the results obtained during second heating have to be considered rather qualitatively.

The activity of CeO2 in GDC-10 and GDC-Zr-5/5 at 1400 °C determined from the first heating by Eq. (1) is 0.92 and 0.91, respectively. Thus, both materials behave like ideal solutions within the measurement accuracy, which was also found in previous measurements [18]. The apparent activity of CeO2 in GDC-10 and GDC-Zr-5/5 at 1400 °C determined from the second heating is 0.81 and 0.48, respectively. This decrease cannot be explained solely by the mass loss of 3 % for GDC-10 and 16 % for GDC-Zr-5/5 during the respective measurements, which is not only attributable to the evaporation of cerium but also of adsorbed water, as the samples were not dried before measurement. All powder samples were sintered to pellets after the measurement. Therefore, it is assumed that the determined activity rather corresponds to the ceria depleted surface of the pellets than to the bulk material. These findings qualitatively support the previous observations that ceria sublimates faster in the initial time when zirconia is present, shown by the higher mass loss of GDC-Zr-5/5 in comparison to GDC-10. After sintering and aging in the first heating cycle, which is accelerated during KEMS measurements in comparison to the annealing experiments due to higher maximum temperature and especially much higher vacuum of  $\sim 10^{-7}$  mbar, sublimation could slow down due to depletion of ceria in the Zr-rich surface region, indicated by the lower apparent activity in the second heating.

## 3.4. Thermal and chemical expansion of GD and GD/Zr doped ceria

Dilatometry enables the determination of thermal and chemical volume changes under variable oxygen partial pressure. The used

samples were polycrystalline in a cubic CaF<sub>2</sub> structure. Thus, it is assumed that volume changes are isotropic and length changes of the sample are directly correlated, to crystal lattice parameters. The thermal expansion  $\epsilon$  was calculated using the temperature-dependent length variation described in Eq. 2. Fig. 18 shows the measured relative length change under air and reducing atmosphere (pO<sub>2</sub>=6  $\times$  10<sup>-7</sup> bar) as a function of temperature for GDC-10 and GDC-Zr-5/5.

To calculate the reversible thermal expansion coefficient of GDC-10 and GDC-Zr-5/5 the thermal length changes of the air measurement  $\varepsilon_T$  up to 1200 °C was used to ensure the absence of chemical expansion. Above 1200 °C the thermal expansion is superimposed by the chemical expansion  $\varepsilon_C$  (Eq. 6) delineated as nonlinearity and instability in  $\varepsilon$  vs. T plots (Fig. 18).

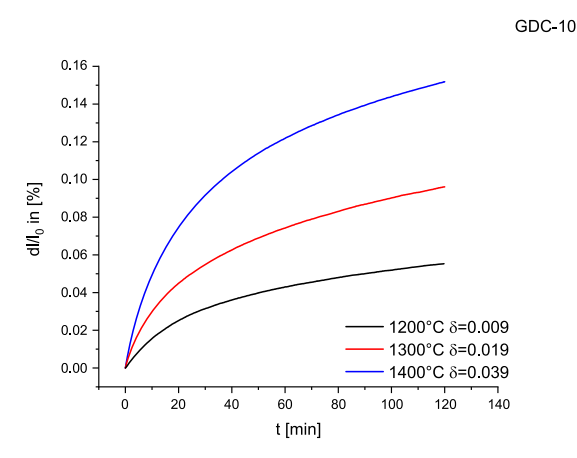
$$\frac{dl}{l_0} = \varepsilon = \varepsilon_T + \varepsilon_C = \alpha_T \Delta T + \alpha_C \Delta \delta \tag{6}$$

The linear coefficients of thermal expansion under air atmosphere (CTE 100-1200  $^{\circ}$ C) are presented in Table 1.

Compared to the undoped cerium oxide [23], the thermal expansion coefficient of GDC-10 is smaller and very close to the value of  $\mathrm{Gd}^{3+}\mathrm{doped}$  ceria of Baral and Tsur [44]. In the case of co-doped ceria, the thermal expansion coefficient is smaller than the coefficients of single doping with trivalent ions. The observed influence of the doping ions on the thermal expansion of ceria must be considered in the design of ceria membranes. As low thermal expansion is a positive factor in terms of reducing stresses, GDC-Zr-5/5 is the preferred material for a membrane here.

Chemical expansion during reduction under low oxygen atmosphere was investigated by isolating chemical and thermal changes using isothermal and non-isothermal reduction conditions. During isothermal conditions the length change of the sample is only due to the reduction-induced chemical expansion of the crystal lattice. The chemical expansion is a result of two competitive phenomena, expansion due to change of cation radii and bond length and contraction due to the formation of oxygen vacancies at higher temperatures [45–48]. For evaluation of the chemical length change the sample was heated to the corresponding target temperature of 1200 °C-1400 °C at a rate of 6 °C/min under vacuum for reduction, and maintained at that level for 120 min for further isothermal reduction. Fig. 19 shows the relative change in length ( $\epsilon$  in %) during the isothermal segment at different temperatures in the range of 1200 °C-1400 °C.

The observed expansion shown here is only the chemical expansion, since it is assumed that the sample does not expand further thermally when the maximum temperature is reached. The expansion for all temperature exhibits similar shapes and differ only in the absolute values for each material. However, a comparison of the materials shows that significantly higher delta values are achieved with a Zr-co doping at a comparably low chemical expansion. For further analysing the curve



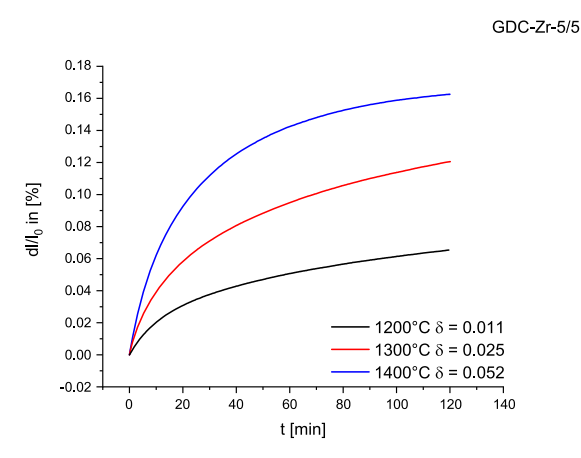
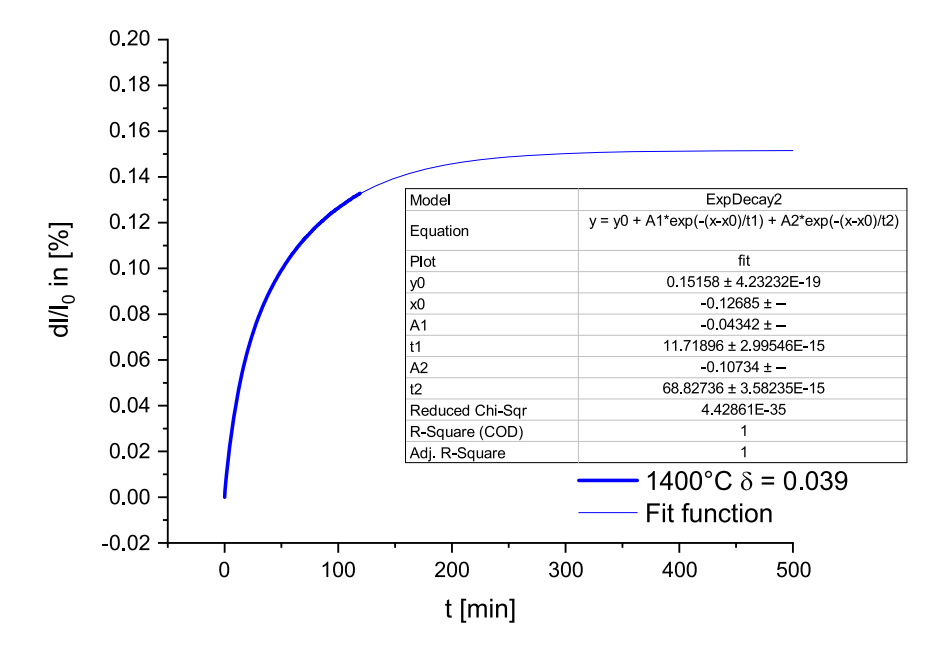


Fig. 19. Isothermal relative length change of GDC-10 and GDC-Zr-5/5 under vacuum (pO $_2$ =6  $\times$  10 $^{-7}$  bar) at 1400 °C, 1300 °C and 1200 °C.

**GDC-10** 





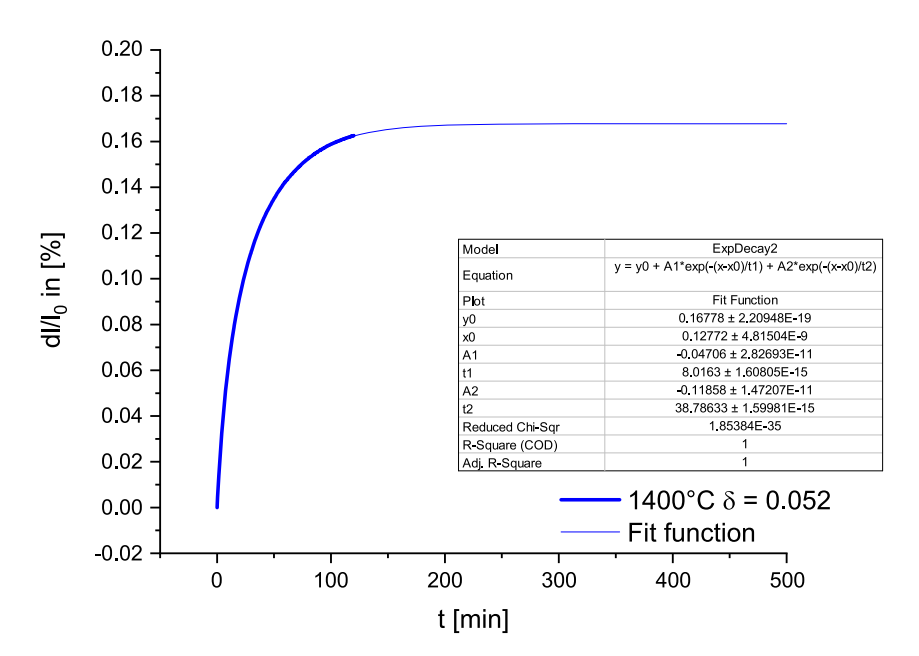


Fig. 20. Relative change in length of GDC-10 and GDC-Zr-5/5 at 1400 °C (pO<sub>2</sub>= $6 \times 10^{-7}$  bar) as function of time. Isothermal time dependence of dl/l<sub>0</sub> where fit by Eq. 7 and extrapolated.

progression in Fig. 20, the experimental data of  $T=1400\,^{\circ}\mathrm{C}$  were fitted with Origin software (OriginLab Inc., USA) using a standard (ExpDecay2) fit equation:

$$y = y_0 + A_1 exp\left(\frac{x - x_0}{t_1}\right) + A_2 exp\left(\frac{x - x_0}{t_2}\right)$$
 (7)

y is here dl/l<sub>0</sub>, the relative change in length and x time t.  $t_1/t_2$  then corresponds to the relaxation time  $\tau_1/\tau_2$ .

The first regime up to dl/ $l_0$ =0.10 % reveals very fast kinetics characterised with a short relaxation time  $\tau 1$  and the second regime with slower kinetics characterised by  $\tau_2$ . Compared to GDC-10, GDC-Zr-5/5 has significantly shorter relaxation times and therefore reaches

equilibrium more quickly. By extrapolating the fit, an equilibrium can be expected after 300 min for GDC-10 and after 200 min for GDC-Zr-5/5. Based on the mathematical relationship between dl/l\_0 and  $\delta$  and pO\_2 at constant temperature, dl/l0 $\propto\!\delta\!\propto\!P_{O2}^n$  [23,49,50] the difference in  $\tau_1/\tau_2$  can be explained by the coefficient n which is higher for the first regime and lower for the second regime. The coefficient n changes by different oxygen vacancy distributions [49]. This behaviour has also been observed in previous studies and is justified by the fact that the oxygen vacancies are statistically distributed at lower  $\delta$  values and are localized in defect complexes at higher  $\delta$  values [17].

For a final evaluation of the chemical length change, it is necessary to consider also the chemical length change during heating. The absolute

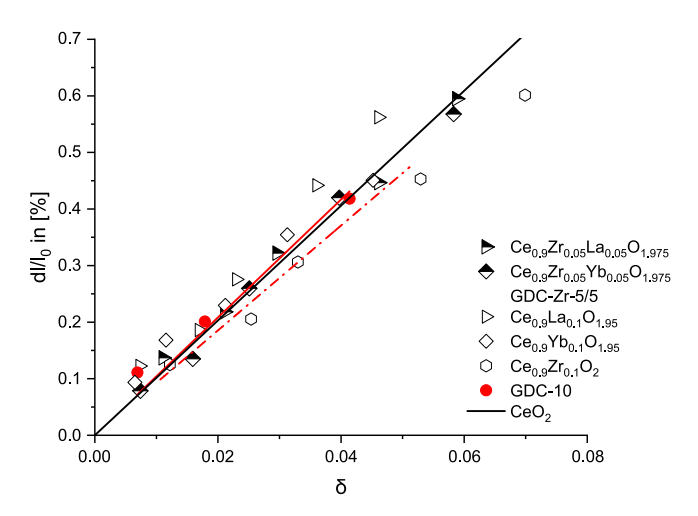


**Fig. 21.** Relative length change as a function of delta of GDC-10 in comparison to data of La, Zr and Yb-doped [17] and undoped ceria [23,51].

**Table 2**The linear coefficients of chemical expansion of GDC-10 and GDC-Zr-5/5 compared to doped ceria in the literature.

Sample	$lpha_c$
CeO <sub>2</sub> [23]	0.10
$Ce_{0.9}La_{0.1}O_{1.95}$ [17]	0.12
$Ce_{0.9}Yb_{0.1}O_{1.95}$ [17]	0.11
$Ce_{0.9}Zr_{0.1}O_2$ [17]	0.087
$Ce_{0.9}Gd_{0.1}O_{1.95}$ [54]	0.14
$Ce_{0.9}Pr_{0.1}O_{1.95}$ [54]	0.087
$Ce_{0.9}Zr_{0.05}La_{0.05}O_{1.975}$ [17]	0.10
$Ce_{0.9}Zr_{0.05}Yb_{0.05}O_{1.975}$ [17]	0.099
GDC-10	0.10
GDC-Zr-5/5	0.093

chemical length change ( $\epsilon_{dynamic} + \epsilon_{isothermal}$ ) as function of reduction extent  $\delta$  is plotted in Fig. 21 in comparison to literature data.

The chemical expansion of GDC-10 is in the range of the chemical expansion of undoped and Yb-doped ceria of our previous study [17] which indicates the influence of dopant radii (La $^{3+}$  = 116 pm, Gd $^{3+}$  = 105.3, Yb $^{3+}$  = 98.5 pm Z = 8 [41]) on the expansion of the crystal lattice. The trivalent doping cations like Gd $^{3+}$  leading to different distances between Ce $^{4+}$  and oxygen vacancies. The repulsion effect increases with increasing ionic radii [17]. In the case of doping with Zr $^{4+}$ , the effect is focusing on oxygen vacancies formed during the reduction. In the present case the chemical expansion is generally lower in comparison to GDC-10 due to the shifting of oxide ions towards oxygen

vacancies facilitated by the smaller ionic radius of Zr<sup>4+</sup> compensating the Ce<sup>4+</sup> relaxation away from the vacancies [52,53]. For classification of the results with literature data on Gd and Zr-doped ceria a linear fitting was performed analogous to the thermal coefficient of expansion by defining a chemical coefficient of expansion:

$$\varepsilon_c = \alpha_c (\delta - \delta_{ref})$$

where  $\epsilon_C$  is the chemical expansion induced by non-stoichiometry  $\delta$  relative to a reference  $\delta_{ref}$  as written in terms of  $\delta$ ,  $\alpha_C$  is a unitless parameter. The  $\alpha_C$  values are presented in Table 2. The calculated  $\alpha_C$  for GDC-10 is close to the value of pure cerium oxide and for GDC-Zr-5/5 between Zr and Gd-doped cerium oxide, as expected.

Beside chemical expansion during reduction also chemical contraction during oxidation was studied. It is assumed that when the prereduced samples are heated under air, they contract during reoxidation and thus the cations and anions relax in the crystal lattice to their original positions. The chemical contraction was measured during second heating of reduced samples under air. The relative changes in length of a pre-reduced GDC-10 sample when reheated in air atmosphere measured with dilatometry are shown below in Fig. 22.

The re-oxidation of GDC-10 occurs very fast and already at temperatures as low as 200 °C. The degree of re-oxidation  $\delta$ , influences the extent of contraction, which relates to the prior expansion during reduction. The re-oxidation temperature is also influenced by  $\delta$  and decreases with increasing  $\delta$ . Commonly, it can be stated that trivalent ions and their additional oxygen vacancies favour re-oxidation through their enhanced diffusion and surface exchange coefficient [55]. The main difference of GDC-10 and GDC-Zr-5/5 contraction could be seen at higher reduction. In the case of GDC-Zr-5/5 it can be observed that re-oxidation occurs in two stages, this is particularly clear for  $\delta$  = 0.052. This interrupted contraction could be a further hint to different substructure phases. It is possible that oxygen vacancies that are present in pyrochlore configuration led to a different contraction during reoxidation than oxygen vacancies in fluorite configuration.

## 4. Conclusions

The present work provides a comprehensive assessment of the mechanisms that limit the long-term stability of  $Gd_{0.1}Ce_{0.9}O_{1.95}$  (GDC-10) under high-temperature ( $\geq 1400~^{\circ}\text{C}$ ) and low-pressure conditions that are typical for solar-thermochemical redox cycles. Prolonged exposure of GDC-10 to a high-vacuum environment ( $\approx 10^{-4}~\text{bar}$ ) at 1400  $^{\circ}\text{C}$  induces pronounced morphological degradation: a porous, spongy surface layer develops as a consequence of the selective sublimation of Cerium. The evolution of this layer follows the Hertz-Knudsen-Langmuir relation and reproduces the behaviour reported by Knoblauch et al. [17].

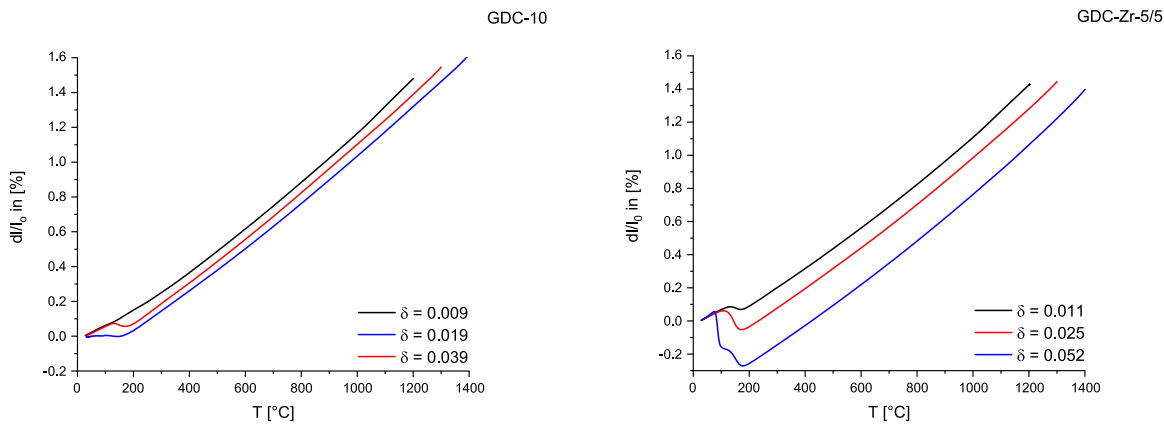


Fig. 22. Relative change in length (ε in %) of GDC-10 during re-oxidation of different reduction states as function of temperature.

In contrast, identical thermal treatments performed in argon at the same temperature and for up to 72 h do not produce comparable porosity, demonstrating that the oxygen partial pressure alone is not the governing parameter. Instead, the total pressure in the vacuum environment is identified as the primary driver of Cerium evaporation and the ensuing surface degradation.

A series of experiments conducted at 1500  $^{\circ}$ C for 72 h confirms that temperature and exposure time are secondary factors; the low total pressure remains the dominant variable. Time-resolved measurements at 1400  $^{\circ}$ C reveal that the extent of surface degradation follows a parabolic kinetic law up to 20 h, indicating a diffusion-controlled process. Energy-dispersive X-ray spectroscopy shows a marked enrichment of Gadolinium around open pores, while closed pores retain the original composition, confirming that Gadolinium accumulates where Cerium is removed

Crystallographic analyses (x-ray diffraction (XRD) and Raman) detect the formation of cubic  $Gd_2O_3$  and monoclinic  $Gd_2SiO_5$  phases, which become more pronounced with increasing exposure time from the heating elements of the furnace.

Building on recent observations by Shugurov [18], the effect of Zr co-doping was investigated by synthesising Ceo.oGdo.osZro.osCO1.osZ (GDC-Zr-5/5) via a sol-gel route. Time-dependent experiments and exponential fitting reveal a thicker, more porous surface layer for the Zr-containing composition, indicative of enhanced Ce<sup>4+</sup> diffusion in earlier stages and limiting after 10 h due phase stabilization. Raman spectroscopy confirms the emergence of a pyrochlore phase in the reduced state, while XRD identifies a cubic Gd-silicate phase and characteristic reflection splitting associated with the co-dopant. Compared with GDC-10, the Zr-doped material exhibits a saturation of surface degradation, suggesting a stabilising effect.

Comparison with Knudsen effusion mass spectrometry and mechanical properties (dilatometry) studies provided further insights into the evaporation mechanism. While the initial  ${\rm CeO_2}$  vapor pressure over GDC-10 and GDC-Zr-5/5 is almost the same, the measured vapor pressure of co-doped samples is significantly lower after aging. Zirconium co-doping reduces chemical expansion, shortens relaxation times, and with this improves mechanical stability during redox cycling. Thermal expansion coefficients determined between 1200 °C and 1400 °C are comparable to literature values, while the chemical contraction observed upon re-oxidation points to more facile diffusion of trivalent ions.

In summary, GDC-10 remains a benchmark material for solar-thermochemical applications, yet its operational durability is compromised under low-pressure environments because of Cerium evaporation and the concomitant surface accumulation of Gadolinium. The integration of Zirconium as a stabilizing dopant presents a viable pathway to mitigate these effects, combining improved thermodynamic stability as well as decreased chemical and thermal expansion coefficients favorable for application with retained ionic conductivity. Future work should focus on quantifying the impact of Zirconium co-doping on actual fuel yield and long-term usage. A special focus should be set on the formed Cerium depletion zone and its effect on the operativity. Another important and critical point is membrane application with thinmembrane layers, which could be impaired really quickly. Further, the testing over multiple redox cycles, as well as optimizing microstructure and reactor design for scalable deployment are recommended.

## CRediT authorship contribution statement

K.T. Streckel: Writing – review & editing, Writing – original draft, Visualization, Methodology, Investigation, Formal analysis, Conceptualization. L. Koch: Writing – review & editing, Methodology, Investigation. M. Müller: Writing – review & editing, Writing – original draft, Investigation. M. Schmitkamp: Writing – review & editing, Investigation. D. Sebold: Writing – review & editing, Investigation. S. Baumann: Writing – review & editing, Project administration, Methodology,

Funding acquisition, Conceptualization. A. Nijmeijer: Writing – review & editing, Supervision. W.A. Meulenberg: Writing – review & editing, Supervision, Resources. N. Knoblauch: Writing – review & editing, Writing – original draft, Visualization, Methodology, Investigation, Formal analysis, Conceptualization.

## Declaration of competing interest

The authors declare the following financial interests/personal relationships which may be considered as potential competing interests: Kevin Timo Streckel reports financial support was provided by Horizon Europe. If there are other authors, they declare that they have no known competing financial interests or personal relationships that could have appeared to influence the work reported in this paper.

#### Acknowledgements

This work has been funded in part by the European Commission under the HORIZON EUROPE project SOMMER HORIZON-CL5-2022-D3-02 under the grant agreement No 101118293 and by the SOL-HYKO research project funded by DLR. The authors gratefully acknowledge Volker Bader for the heat treatments and performance of the annealing tests, Michael Xhonneux for assisting and preparing metallographic cross sections, Stefan Heinz for his technical assistance in sample preparation and Torben Reuter for assistance in measuring Raman spectra.

## Supplementary materials

Supplementary material associated with this article can be found, in the online version, at doi:10.1016/j.oceram.2025.100871.

## References

- M. Roeb, C. Sattler, Hydrogen and hydrocarbon fuels from abundant resources and solar energy: current activities and perspectives in DLR's institute of future fuels, J. Phys. 2812 (2024) 012005, https://doi.org/10.1088/1742-6596/2812/1/ 012005
- [2] A. Ikram, M. Zulfequar, V.R. Satsangi, Role and prospects of green quantum dots in photoelectrochemical hydrogen generation: a review, Int. J. Hydrog. Energy 47 (2022) 11472–11491, https://doi.org/10.1016/j.ijhydene.2022.01.187.
- [3] J.R. Scheffe, D. Weibel, A. Steinfeld, Lanthanum-strontium-manganese perovskites as redox materials for solar thermochemical splitting of H<sub>2</sub>O and CO<sub>2</sub>, Energy Fuels 27 (2013) 4250–4257, https://doi.org/10.1021/ef301923h.
- [4] W.C. Chueh, C. Falter, M. Abbott, D. Scipio, P. Furler, S.M. Haile, et al., High-flux solar-driven thermochemical dissociation of CO<sub>2</sub> and H<sub>2</sub>O using nonstoichiometric ceria, Science 330 (2010) 1797–1801, https://doi.org/10.1126/science.1197834.
- [5] M. Tou, R. Michalsky, A. Steinfeld, Solar-driven thermochemical splitting of CO2 and in situ separation of CO and O2 across a ceria redox membrane reactor, Joule 1 (2017) 146–154, https://doi.org/10.1016/j.joule.2017.07.015.
- [6] A. Haeussler, S. Abanades, J. Jouannaux, A. Julbe, Demonstration of a ceria membrane solar reactor promoted by dual perovskite coatings for continuous and isothermal redox splitting of CO2 and H2O, J. Memb. Sci. 634 (2021) 119387, https://doi.org/10.1016/j.memsci.2021.119387.
- [7] M. Tou, J. Jin, Y. Hao, A. Steinfeld, R. Michalsky, Solar-driven co-thermolysis of CO<sub>2</sub> and H<sub>2</sub> O promoted by in situ oxygen removal across a non-stoichiometric ceria membrane, React. Chem. Eng. 4 (2019) 1431–1438, https://doi.org/ 10.1039/C8RE00218E.
- [8] K. Lee, N. Knoblauch, C. Agrafiotis, M. Pein, M. Roeb, M. Schmücker, et al., Strategic co-doping of ceria for improved oxidation kinetics in solar thermochemical fuel production, Mater. Today Energy 35 (2023) 101321, https://doi.org/10.1016/j.mtener.2023.101321.
- [9] A. Lidor, B. Bulfin, A critical perspective and analysis of two-step thermochemical fuel production cycles, Solar Compass 11 (2024) 100077, https://doi.org/ 10.1016/j.solcom.2024.100077.
- [10] R. Kiebach, S. Pirou, L. Martinez Aguilera, A.B. Haugen, A. Kaiser, P.V. Hendriksen, et al., A review on dual-phase oxygen transport membranes: from fundamentals to commercial deployment, J. Mater. Chem. A 10 (2022) 2152–2195, https://doi.org/10.1039/D1TA07898D.
- [11] M. Takacs, J.R. Scheffe, A. Steinfeld, Oxygen nonstoichiometry and thermodynamic characterization of Zr doped ceria in the 1573–1773 K temperature range, Phys. Chem. Chem. Phys. 17 (2015) 7813–7822, https://doi. org/10.1039/c4cp04916k.
- [12] M. Laqdiem, A.J. Carrillo, G. Dimitrakopoulos, M. Balaguer, J. Garcia-Fayos, A. F. Ghoniem, et al., Impact of lattice properties on the CO2 splitting kinetics of

- lanthanide-doped cerium oxides for chemical looping syngas production, Solid. State Ion. 394 (2023) 116192, https://doi.org/10.1016/j.ssi.2023.116192.
- [13] M. Hoes, C.L. Muhich, R. Jacot, G.R. Patzke, A. Steinfeld, Thermodynamics of paired charge-compensating doped ceria with superior redox performance for solar thermochemical splitting of H<sub>2</sub>O and CO<sub>2</sub>, J. Mater. Chem. A 5 (2017) 19476–19484, https://doi.org/10.1039/c7ta05824a.
- [14] C.L. Muhich, B.W. Evanko, K.C. Weston, P. Lichty, X. Liang, J. Martinek, et al., Efficient generation of H<sub>2</sub> by splitting water with an isothermal redox cycle, Science 341 (2013) 540–542, https://doi.org/10.1126/science.1239454.
- [15] R. Schäppi, D. Rutz, F. Dähler, A. Muroyama, P. Haueter, J. Lilliestam, et al., Dropin fuels from sunlight and air, Nature 601 (2022) 63–68, https://doi.org/10.1038/ s41586-021-04174-y
- [16] S. Zoller, E. Koepf, D. Nizamian, M. Stephan, A. Patané, P. Haueter, et al., A solar tower fuel plant for the thermochemical production of kerosene from H2O and CO2, Joule 6 (2022) 1606–1616, https://doi.org/10.1016/j.joule.2022.06.012.
- [17] N. Knoblauch, K. Lee, G. Alkan, P. Mechnich, M. Pein, C. Agrafiotis, et al., Chemical expansion of La3+ and Yb3+ incorporated Zr-doped ceria ceramics for concentrated solar energy-driven thermochemical production of fuels, Solid. State Ion. 405 (2024) 116451, https://doi.org/10.1016/j.ssi.2023.116451.
- [18] S.M. Shugurov, O.A. Zhinkina, E.A. Balabanova, D.A. Repin, S.I. Lopatin, CeO2-Gd2O3 system: evaporation and thermodynamics, Ceram. Int. 51 (2025) 7202–7207, https://doi.org/10.1016/j.ceramint.2024.12.154.
- [19] Raksha Sharma, Growth Market Reports, Shruti Bhat. Gadolinium-Doped Ceria Electrolyte Market Research Report 2033. Growth Market Reports n.d. https://gro wthmarketreports.com/report/gadolinium-doped-ceria-electrolyte-market (Accessed 7 October 2025).
- [20] V. Loddo, S. Yurdakal, F. Parrino, Economical aspects, toxicity, and environmental fate of cerium oxide. Cerium Oxide (CeO<sub>2</sub>): Synthesis, Properties and Applications, Elsevier, 2020, pp. 359–373, https://doi.org/10.1016/B978-0-12-815661-2.00009-8
- [21] M.P. Pechini. Method of preparing lead and alkaline earth titanates and niobates and coating method using the same to form a capacitor. 3330697, 1968.
- [22] U. Schulz, B. Saruhan, K. Fritscher, C. Leyens, Review on advanced EB-PVD ceramic topcoats for TBC applications, Int. J. Appl. Ceram. Tech. 1 (2004) 302–315, https://doi.org/10.1111/j.1744-7402.2004.tb00182.x.
- [23] N. Knoblauch, H. Simon, M. Schmücker, Chemically induced volume change of CeO2–δ and nonstoichiometric phases, Solid. State Ion. 301 (2017) 43–52, https://doi.org/10.1016/j.ssi.2017.01.003.
- [24] N. Knoblauch, H. Simon, L. Dörrer, D. Uxa, S. Beschnitt, P. Fielitz, et al., Ceria: recent results on dopant-induced surface phenomena, Inorganics 5 (2017) 76, https://doi.org/10.3390/inorganics5040076.
- [25] M. Bond, H. Struchtrup, Mean evaporation and condensation coefficients based on energy dependent condensation probability, Phys. Rev. E 70 (2004) 061605, https://doi.org/10.1103/PhysReyE.70.061605.
- [26] J. Jurczyk, C. Glessi, K. Madajska, L. Berger, J.I.K. Nyrud, I. Szymańska, et al., Vacuum versus ambient pressure inert gas thermogravimetry: a study of silver carboxylates, J. Therm. Anal. Calorim. 147 (2022) 2187–2195, https://doi.org/ 10.1007/s10973-021-10616-6
- [27] M. Kaufman, Principles of Thermodynamics, Marcel Dekker, New York, 2002.
- [28] S.J. Hong, A.V. Virkar, Lattice parameters and densities of rare-earth oxide doped ceria electrolytes, J. Am. Ceram. Soc. 78 (1995) 433–439, https://doi.org/ 10.1111/j.1151-2916.1995.tb08820.x.
- [29] M. Guo, J. Lu, Y. Wu, Y. Wang, M. Luo, UV and visible Raman studies of oxygen vacancies in rare-earth-doped ceria, Langmuir 27 (2011) 3872–3877, https://doi. org/10.1021/la200292f.
- [30] K. Lee, J.R. Scheffe, Characterization of a laser-based heating system coupled with in operando Raman spectroscopy for studying solar thermochemical redox cycles, J. Sol. Energy Eng. 141 (2019) 021013, https://doi.org/10.1115/1.4042229.
- [31] T. Taniguchi, T. Watanabe, N. Sugiyama, A.K. Subramani, H. Wagata, N. Matsushita, et al., Identifying defects in ceria-based nanocrystals by UV resonance Raman spectroscopy, J. Phys. Chem. C 113 (2009) 19789–19793, https://doi.org/10.1021/jip9049457.
- [32] S. Loridant, Raman spectroscopy as a powerful tool to characterize ceria-based catalysts, Catal. Today 373 (2021) 98–111, https://doi.org/10.1016/j. cattod 2020.03.044
- [33] P. EYu, A.A. Murashkina, V.I. Maragou, A.K. Demin, V.N. Strekalovsky, P. E. Tsiakaras, CeO2 based materials doped with lanthanides for applications in intermediate temperature electrochemical devices, Int. J. Hydrog. Energy 36 (2011) 6175–6183, https://doi.org/10.1016/j.ijhydene.2011.01.132.

- [34] R. Schmitt, A. Nenning, O. Kraynis, R. Korobko, A.I. Frenkel, I. Lubomirsky, et al., A review of defect structure and chemistry in ceria and its solid solutions, Chem. Soc. Rev. 49 (2020) 554–592, https://doi.org/10.1039/C9CS00588A.
- [35] W.H. Weber, K.C. Hass, J.R. McBride, Raman study of CeO 2: second-order scattering, lattice dynamics, and particle-size effects, Phys. Rev. B 48 (1993) 178–185, https://doi.org/10.1103/PhysRevB.48.178.
- [36] K. Kuntaiah, P. Sudarsanam, B.M. Reddy, A. Vinu, Nanocrystalline Ce1-xSmxO2-δ (x = 0.4) solid solutions: structural characterization versus CO oxidation, RSC Adv. 3 (2013) 7953, https://doi.org/10.1039/c3ra23491f.
- [37] R.C. Maher, L.F. Cohen, P. Lohsoontorn, D.J.L. Brett, N.P. Brandon, Raman spectroscopy as a probe of temperature and oxidation state for gadolinium-doped ceria used in solid oxide fuel cells, J. Phys. Chem. A 112 (2008) 1497–1501, https://doi.org/10.1021/jp0763611.
- [38] J. Yu, L. Cui, H. He, S. Yan, Y. Hu, H. Wu, Raman spectra of RE2O3 (RE=Eu, Gd, Dy, Ho, Er, Tm, Yb, Lu, Sc and Y): laser-excited luminescence and trace impurity analysis, J. Rare Earths 32 (2014) 1–4, https://doi.org/10.1016/S1002-0721(14) 60025-9.
- [39] M. Gao, P. Zhang, L. Luo, R. Guo, Y. Wang, Structural and optical characterization of Gd2SiO5:Tb3+ crystal obtained by optical floating zone method, Optik 225 (2021) 165814, https://doi.org/10.1016/j.ijleo.2020.165814.
- [40] S.N. Achary, S.K. Sali, N.K. Kulkarni, P.S.R. Krishna, A.B. Shinde, A.K. Tyagi, Intercalation/deintercalation of oxygen: a sequential evolution of phases in Ce<sub>2</sub> O<sub>3</sub> /CeO<sub>2</sub> –ZrO<sub>2</sub> pyrochlores, Chem. Mater. 21 (2009) 5848–5859, https://doi.org/ 10.1021/cm902450q.
- [41] R.D. Shannon, Revised effective ionic radii and systematic studies of interatomic distances in halides and chalcogenides, Acta Cryst. A 32 (1976) 751–767, https://doi.org/10.1107/S0567739476001551.
- [42] A.R. Cleave, Atomic Scale Simulations For Waste Form Applications, Department of Materials Imperial College of Science, Technology and Medicine University of London, 2006.
- [43] B.P. Mandal, M. Pandey, A.K. Tyagi, Gd2Zr2O7 pyrochlore: potential host matrix for some constituents of thoria based reactor's waste, J. Nucl. Mater. 406 (2010) 238–243, https://doi.org/10.1016/j.jnucmat.2010.08.042.
- [44] A.K. Baral, Y. Tsur, Investigation of thermo-chemical expansions in Pr and Gd doped ceria by a novel temperature modulated dilatometry approach, J. Eur. Ceram. Soc. 42 (2022) 2299–2306, https://doi.org/10.1016/j.jeurceramsoc.2021.12.040.
- [45] D. Marrocchelli, S.R. Bishop, H.L. Tuller, B. Yildiz, Understanding chemical expansion in non-stoichiometric oxides: ceria and zirconia case studies, Adv. Funct. Mater. 22 (2012) 1958–1965, https://doi.org/10.1002/adfm.201102648.
- [46] D. Marrocchelli, S.R. Bishop, J. Kilner, Chemical expansion and its dependence on the host cation radius, J. Mater. Chem. A 1 (2013) 7673, https://doi.org/10.1039/ c3ta11020f
- [47] S.R. Bishop, Chemical expansion of solid oxide fuel cell materials: a brief overview,
   Acta Mech. Sin. 29 (2013) 312–317, https://doi.org/10.1007/s10409-013-0045-y.
   [48] C.L. Muhich, Re-evaluating CeO<sub>2</sub> expansion upon reduction: noncounterpoised
- [48] C.L. Munich, Re-evaluating CeO<sub>2</sub> expansion upon reduction: noncounterpoise forces, not ionic radius effects, are the cause, J. Phys. Chem. C 121 (2017) 8052–8059, https://doi.org/10.1021/acs.jpcc.6b12373.
- (49) O.T. Sørensen, Thermodynamic studies of the phase relationships of nonstoichiometric cerium oxides at higher temperatures, J. Solid. State Chem. 18 (1976) 217–233, https://doi.org/10.1016/0022-4596(76)90099-2.
- [50] R.J. Panlener, R.N. Blumenthal, J.E. Garnier, A thermodynamic study of nonstoichiometric cerium dioxide, J. Phys. Chem. Solids 36 (1975) 1213–1222, https://doi.org/10.1016/0022-3697(75)90192-4.
- [51] N. Knoblauch, Synthese, Charakterisierung und Untersuchung zum Redoxverhalten von Ceroxidbasierten Materialien zur Erzeugung Solarer Brennstoffe, TU Clausthal, 2018.
- [52] S.R. Bishop, T. Nakamura, K. Amezawa, Chemically-induced expansion of Zr0.2Ce0.802-8, Solid. State Ion. 261 (2014) 1-4, https://doi.org/10.1016/j. cci.2014.02.005
- [53] S.R. Bishop, D. Marrocchelli, W. Fang, K. Amezawa, K. Yashiro, G.W. Watson, Reducing the chemical expansion coefficient in ceria by addition of zirconia, Energy Environ. Sci. 6 (2013) 1142, https://doi.org/10.1039/c3ee23917a.
- [54] S.R. Bishop, K.L. Duncan, E.D. Wachsman, Defect equilibria and chemical expansion in non-stoichiometric undoped and gadolinium-doped cerium oxide, Electrochim. Acta 54 (2009) 1436–1443, https://doi.org/10.1016/j. electacta.2008.09.026.
- [55] D. Uxa, L. Dörrer, M. Schulz, N. Knoblauch, P. Fielitz, M. Roeb, et al., Investigation of CO2 splitting on ceria-based redox materials for low-temperature solar thermochemical cycling with oxygen isotope exchange experiments, Processes 11 (2022) 109, https://doi.org/10.3390/pr11010109.